

# Substructure, supernovae, and a time-resolved star formation history for Upper Scorpius

Geovanny Briceño-Morales,<sup>1,2\*</sup> Julio Chanamé<sup>2</sup>

<sup>1</sup>*Centro de Investigaciones Espaciales (CINESPA), Escuela de Física, Universidad de Costa Rica, San Pedro de Montes de Oca 11501, San José, Costa Rica*

<sup>2</sup>*Instituto de Astrofísica, Pontificia Universidad Católica de Chile, Av. Vicuña Mackenna 4860, 782-0436 Macul, Santiago, Chile*

Accepted 2023 February 15. Received 2023 February 13; in original form 2022 May 03

## ABSTRACT

The improved astrometry precision of Gaia-eDR3 allows us to perform a detailed study of the Upper Scorpius OB association and revisit its spatial, kinematic, and age substructure. We achieve this by combining clustering techniques and complementing with age estimations based on Gaia photometry. Our census retrieves 3661 candidate members for Upper Scorpius with contamination  $\sim 9\%$ . We also extract an astrometrically clean sample of 3004 sources with contamination  $\sim 6\%$ . We show that Upper Scorpius can be divided into at least 3 main kinematic groups. We systematically investigate and characterize the Upper Scorpius' internal structure, revealing that at least  $\sim 34\%$  of its stellar populations are contained in 7 spatial substructures, with well defined boundaries, kinematics and relative ages, with suggested names:  $\pi$  Scorpii ( $20^{+2}_{-1}$  Myr),  $\alpha$  Scorpii ( $14^{+2}_{-1}$  Myr),  $\delta$  Scorpii ( $9^{+2}_{-1}$  Myr),  $\beta$  Scorpii ( $8^{+1}_{-1}$  Myr),  $\omega$  Scorpii ( $8^{+1}_{-1}$  Myr),  $\nu$  Scorpii ( $7^{+1}_{-1}$  Myr), after their brightest member, and the well known  $\rho$  Ophiuchi ( $4^{+1}_{-1}$  Myr). We find a clear correlation in (1) density-age, providing an empirical expansion law to be tested in other associations, and (2) tangential velocity-age, providing constraints on the dynamics of these substructures and the position of potential past triggering events. We estimate the time at which 4 potential supernovae events occurred in Upper Scorpius. Based on these findings, we tie together previous work on the region and suggest a star formation history with unprecedented temporal resolution.

**Key words:** stars: pre-main sequence, supernovae – galaxy: kinematics and dynamics, open clusters and associations – astrometry and celestial mechanics

## 1 INTRODUCTION

OB associations are loose groups of young stars and young stellar objects with prominent OB stars as members. These structures have long been thought to be an intermediate stage between star formation and the less dense young populations of the Galactic field (Blaauw 1964). Hence, observations of nearby OB associations are fundamental for the test and proposal of models ranging from the early stages of stellar evolution to the structure, composition and dynamics of the Galactic populations. In this context, Upper Scorpius (USco) has a great importance as it is thought to be the youngest group of the three conforming the Scorpius-Centaurus OB2 association (Sco-Cen), the nearest to Earth (e.g., de Geus 1992; de Zeeuw et al. 1999; Pecaute & Mamajek 2016) and one of the nearest places ( $\sim 140$  pc) that show evidence of active or recent star formation (de Zeeuw et al. 1997; Preibisch & Mamajek 2008; Pillitteri et al. 2016). Therefore, in depth efforts have been made in order to provide a systematic characterization of the stellar populations in USco.

Before the Gaia mission (Gaia Collaboration et al. 2016), only mid to high-mass members were properly identified via astrometric methods, while the expected low mass populations were obtained mainly with photometric and spectroscopic methods (Wright 2020), yielding important insights on its features (e.g., Preibisch & Zin-

necker 1999; Lodieu et al. 2013) but keeping them without a precise description of their astrometric properties. However, pre-Gaia studies were enough to unveil puzzling characteristics of USco like its broad age dispersion (Pecaute et al. 2012) and complicated structure (Pecaute & Mamajek 2016; Wright & Mamajek 2018), leading to the proposal of multiple scenarios to explain this (e.g., Feiden 2016; David et al. 2019; Sullivan & Kraus 2021).

Several studies have been done to update the USco low mass populations membership revealed by the Gaia data (e.g., Cook et al. 2017; Wilkinson et al. 2018; Damiani et al. 2019; Luhman & Esplin 2020; Luhman 2022), as it provides unprecedented completeness and precision in its five parameter (sky position, parallax and proper motion) astrometrical solution. However, until recently, no one had been able to characterize in a systematic way the internal structure of USco as revealed by this data, mostly due to the apparently high level of mixing seen on its internal stellar populations that does not seem to show any pattern in the spatial nor kinematic spaces (Damiani et al. 2019). The latter was partially solved by the recent work of Kerr et al. (2021), where the authors use the HDBSCAN clustering algorithm to successfully find and characterize young substructures up to a distance of  $\sim 333$  pc around the Sun, including substructure in Sco-Cen and USco. However, even though the work of Kerr et al. (2021) provides an important first insight on the properties of USco, this particular implementation of HDBSCAN is affected by the definition of the clustering space when resolving the very local spatial

\* E-mail: gbriceno@astro.puc.cl

and kinematic substructure of USco, as we will discuss in Section (3.2.1). This is further affected by the lower precision of the Gaia DR2 with respect to the Gaia eDR3 catalogue, i.e., the typical errors in Gaia DR2 (Gaia Collaboration et al. 2018) are larger by a factor of  $\sim 3$  in proper motion and 30-50% in parallax. More recently, Squicciarini et al. (2021) found kinematic evidence of substructure in USco by tracing back the positions of USco candidate members. Via this approach, the authors were able to recover substructures that visually resemble some of the retrieved by Kerr et al. (2021). However, a robust validation and in depth characterization of these substructures, if validated, has not been performed yet. Another open problem in USco is that age estimations yield a rather broad age dispersion (e.g., Pecaut & Mamajek 2016; Luhman 2022) and, until now, there was no clear pattern in the ages of the local USco substructures found with Gaia. We will show that this age problem has a natural solution if a multidimensional analysis is performed, systematic effects are considered when extracting isochronal ages and the massive membership and concrete past supernovae events in USco, if any, are investigated. In short, we aim to contribute with an in depth and systematic characterization of the internal structure of USco to extract new information about this important region, all based solely on the Gaia eDR3 catalogue (Gaia Collaboration et al. 2020).

This work is organized as follows: in Section 2, we summarize the limits that contain our main data set of the USco region, define some useful notation and describe the subsample of massive stars. In Section 3 we describe: the Kinematic Analysis, i.e., the implementation of the Gaussian Mixture (GM) fit (Pedregosa et al. 2011) to identify kinematic groups (KGs) in velocity space with a Bayesian approach, the Spatial Analysis, where we use OPTICS (Ankerst et al. 1999) to directly see the internal structure of USco in the (X,Y,Z) Galactic Heliocentric Coordinates and the Time Analysis, where we investigate the input parameters of the present-day mass function in order to estimate the number and time of supernovae events occurred in USco. In Section 4, we show that this approach from multiple directions proves to be useful because it gives new detailed and relevant information about the substructure, kinematics, dynamics, age, star formation history of USco and yields new constraints in the fundamental properties of its massive members. In Section 6 we summarize and discuss our results in relation with the age and past supernovae events in USco to suggest a star formation scenario with unprecedented temporal resolution.

## 2 DATA AND NOTATION

### 2.1 Gaia

We download all Gaia eDR3 sources contained within the sky region defined by de Zeeuw et al. (1997), in Galactic coordinates ( $\ell, b$ ), and closer than 200 pc according to the (inverse of) eDR3 parallax ( $\varpi$ ). That is:

$$343^\circ < \ell < 360^\circ \quad (1)$$

$$10^\circ < b < 30^\circ \quad (2)$$

$$\varpi > 5 \text{ mas} \quad (3)$$

The upper distance of  $\sim 200$  pc is taken following Damiani et al. (2019) (its Sect.5.3). Distance estimation by inversion of the parallax constitutes a good approximation at the distance of our analysis (Luri et al. 2018). The resulting data set contains 51689 sources and we will refer to it as the Raw Gaia-eDR3 set. We aim to compile a

complete sample of candidate members from this set, but the nature of the analysis in this work requires a small-error subset. Hence, we apply the following quality criteria (Lindgren et al. 2021) on the Raw Gaia-eDR3 set's parameters:

$$\varpi/\text{error}_\varpi > 10 \quad (4)$$

$$\text{RUWE} < 1.4 \quad (5)$$

where the upper limit in RUWE provides a highly clean five-parameter solution (Lindgren et al. 2018). The resulting data set is composed by 17535 sources and we refer to it as Gaia-eDR3 set.

Furthermore, we refer to the sample from the Gaia-eDR3 set with available radial velocities ( $V_r$ ) as the Gaia-eDR3 $_{V_r}$  sample (2310 sources). The distinction is necessary as only the latter sample can be fully described in the (U,V,W) space. To describe the kinematic properties of sources with no  $V_r$  measurements, we use the tangential velocity offset ( $V_{T*}$ ) obtained after correcting perspective effects from the tangential velocities ( $V_T$ ) (see Appendix A), which is necessary due to the large sky area under study ( $\sim 340$  sq.deg.). We work in the Galactic Cartesian heliocentric positions (X,Y,Z), with axes pointing to:

- X (pc): Galactic center
- Y (pc): direction of Galactic rotation
- Z (pc): North Galactic Pole

and the respective Galactic Cartesian velocities (U,V,W) km s $^{-1}$ . We also denote the other main kinematic variables as:

- $\mu_i$  (mas yr $^{-1}$ ): i component of the proper motion
- $V_i$  (km s $^{-1}$ ): i component of the tangential velocity
- $V_{iexp}$  (km s $^{-1}$ ): i component of the expected tangential velocity

### 2.2 Massive stars

We also investigate the relation between the most massive stars from USco and its internal substructure. In order to do this, we compile a sample with the turn-off stars in USco from Pecaut & Mamajek (2016) (its Table 10) plus Antares ( $\alpha$  Sco $_{\star}$ )<sup>1</sup> and we refer to this as the Turn-off sample. There are four stars with no  $\varpi$  or  $\mu$  measurements from Gaia: Antares, Dschubba ( $\delta$  Sco $_{\star}$ ), Paikauhale ( $\tau$  Sco $_{\star}$ ) and Alniyat ( $\sigma$  Sco $_{\star}$ ). We use astrometry from HIPPARCOS (van Leeuwen 2007) for these stars. In the particular case of Alniyat, we use the improved distance from North et al. (2007) and estimate its  $V_T$  based on it.

## 3 METHODS

It is convenient to divide our analysis in three main branches clearly distinguished by the spaces where they are developed into; the Kinematic, Spatial and Time analysis. Later, we will see how the information obtained from each space merges to tie and constrain our knowledge about USco.

<sup>1</sup> To avoid confusion in further sections, we will refer to these stars by their approved names (see [https://www.iau.org/public/themes/naming\\_stars/](https://www.iau.org/public/themes/naming_stars/)), or include the sub index " $\star$ " in their Bayer designation.

### 3.1 Kinematic Analysis

By taking advantage of the high precision astrometry of the Gaia-eDR3 data, we perform a variation of the Convergent Point method, as implemented by [Perryman et al. \(1998\)](#), that intends to allow us to distinguish kinematic substructures in USco, if any, and their respective spatial distributions and ages. We will refer to the application of this method as the Kinematic Analysis and we explain it and summarize it as follows.

1. The existence of an OB association and its presence in the data implies two fundamental facts: OB stars must be present and they must have similar kinematic properties. To assess this, we search for OB stars in our Raw Gaia-eDR3 set. This can be done by performing a nearest neighbor sky crossmatch of the OB stars catalog from [Gontcharov \(2012\)](#) with this set. We also aim to obtain a more complete sample by transforming the observed color index to the intrinsic spectral type of the stars, we opt to do this making use of the intrinsic Gaia colors from [Luhman \(2022\)](#) and near-IR color- $T_{\text{eff}}$  estimates for O9V-M9V MS stars from [Pecaut & Mamajek \(2013\)](#) (its Table 5)<sup>2</sup>. For the latter, we crossmatch the set with the near-IR 2MASS catalog ([Skrutskie et al. 2006](#)) and select the OB stars according to the corrections of [Pecaut & Mamajek \(2013\)](#). We complement our selection with the stars contained in the Turn-Off sample (see Section 2.2) and double check with the catalog from [Skiff \(2009\)](#). With this method, we expect to obtain a complete sample of stars with spectral type (SpT) < B0. We refer to the final sample of OB stars candidates (plus Antares) as the OB sample.

2. To identify the underlying stellar populations related to a group of clustered OB stars, if any, in a given kinematic space, we fit the velocity distribution of the Gaia-eDR3 set with a GM model. For the Gaia-eDR3<sub>V<sub>r</sub></sub> sample, we are able to apply the GM fit ([Pedregosa et al. 2011](#)) to the data in the (U,V,W) space. The number of components of the fit is chosen according to the Bayesian Information Criterion (BIC) (see Appendix B). If none or only a few OB stars have available V<sub>r</sub> measurements, the component that corresponds to the OB association, if any, can be recognized by comparing with the respective positions of the OB stars in the V<sub>T</sub> space, so that we choose the one (or the ones) that better overlap with the OB sample's velocity distribution and study its physical properties. The mean (U,V,W) values of the selected component can be identified with the true barycenter motion of the association (see Appendix A). We refer to this step in the Kinematic Analysis as the First GM fit and Figure 1 shows the result of applying it to the OB and Gaia-eDR3<sub>V<sub>r</sub></sub> samples.

3. Formally, the stars have to be clustered in the (U,V,W) velocity space, but most (~88%) of the data in the (Raw) Gaia-eDR3 data do not have available V<sub>r</sub> measurements, so we have to deal in a different way with these sources. We do this by applying the GM fit a second time in the V<sub>T</sub>\* space, which is calculated via the true barycenter motion retrieved from the First GM fit (see Appendix A). We run this Second GM fit in the V<sub>T</sub>\* space for the (Raw) Gaia-eDR3 set with the the number of components given by the BIC. In this space, the association's members are expected to be near the origin, hence, we select the component with mean V<sub>T</sub>\* ~ (0,0). Moreover, we can calculate the posterior probabilities for each star to belong to the selected component, hence, we are able to select a confidence region, depending on the desired precision, to perform the rest of the analysis. We will refer to the final confidence region of the selected component from the (Raw) Gaia-eDR3 set as the (Raw) USco KG,

which constitute the candidate members' census of the OB association.

4. We can further look for kinematic substructures that could not be obtained in the Second GM fit on the V<sub>T</sub>\* space<sup>3</sup>. The procedure is the same as before with the only difference that the fit is performed on the USco KG rather than the Gaia-eDR3 set. We rely on the BIC criteria for this new fit to say if the selected component is better modeled with a new mixture of components or not, and interpret the results as a suggestion of the absence or presence of kinematic substructures within the USco KG.

This approach overcomes the necessity of relying on previous results about the presence and kinematic properties of an OB association and allows us to look for kinematic substructures instead of assuming only one KG. Furthermore, the method keeps the advantage of not having to make any assumptions about the spatial distribution of the OB association, so that not only spatially clustered stars are taken as members but also spatially diffuse candidates are included ([Perryman et al. 1998](#)). This is an advantage when dealing with OB associations as they are not necessarily spatially dense populations.

#### 3.1.1 Contamination and mixing

The GM fit also allows us to estimate not only the level of contamination from field stars but also the internal mixing percentile of the KGs, if present, based on the fitted distributions associated to each one of them. The correspondent posterior probabilities can be calculated for each star with the Bayes theorem:

$$P(KG_i|V_{T*}) = \frac{P(V_{T*}|KG_i) \cdot P(KG_i)}{P(V_{T*})} \quad (6)$$

Here  $P(KG_i|V_{T*})$  is the posterior probability for a star to belong to the i-th component fitted, i.e., the i-th KG, given a position in the V<sub>T</sub>\* space. The likelihood  $P(V_{T*}|KG_i)$ , the prior  $P(KG_i)$  and the normalization constant  $P(V_{T*})$  are obtained with the sci-kit learn GM fit implementation ([Pedregosa et al. 2011](#)). The percentiles representing how many stars from the i-th KG are in a given region of the V<sub>T</sub>\* space, can be calculated as

$$\%_{mix} = \frac{P(KG_i|V_{T*})}{\sum_i P(KG_i|V_{T*})} \quad (7)$$

This is the mixing between different components or KGs, which may refer to the Galactic field, the association's sources or, if present, the internal mixing of the association's kinematic substructures. However, this implementation has as major limitations that it is based on the strong assumption of the data to be normal-distributed, and that it does not take into account the errors involved. In particular, the latter assumption may lead to systematic biases if the typical errors are in the same order of magnitude than 1σ of the smallest component fitted by the model ([Ivezić et al. 2014](#)).

As we will show, the Kinematic Analysis proves to be useful when separating USco from the Galactic field, and allows for further spatial substructure to become apparent, but fails to resolve it cleanly. Hence, we need to complement with a clustering algorithm which is able to resolve this substructure, while dealing with noise, and making no prior assumptions about the distribution or density of a cluster, if any, in the space under analysis. We describe such method in the following section.

<sup>2</sup> An updated version of the table can be found at [https://www.pas.rochester.edu/~emamajek/EEM\\_dwarf\\_UBVIJHK\\_colors\\_Teff.txt](https://www.pas.rochester.edu/~emamajek/EEM_dwarf_UBVIJHK_colors_Teff.txt)

<sup>3</sup> This may happen if the true over densities are too local or if they are too close from each other.

### 3.2 Spatial analysis

The OPTICS algorithm (Pedregosa et al. 2011) is a density-based clustering technique that allows to directly see the intrinsic density structure of any  $n$ -dimensional data set via its Reachability (R) plot (Ankerst et al. 1999). We opt to implement OPTICS in our analysis because of its great advantage of not assuming a number of present clusters or any prior distribution on the data and because of its ability to extract clusters with different densities. Here, we introduce the main concepts involved and a guide for the interpretation of the R plot. For a thorough exposition and a recent implementation in the  $\rho$  Ophiuchi region see Ankerst et al. (1999) and Cánovas et al. (2019), respectively.

#### 3.2.1 Fundamental concepts

The local density of an  $n$ -dimensional data set can be defined as the number of points inside a given radius  $\epsilon$ . A core point  $o$ , then, is defined as a local point that minimizes  $\epsilon$  for a given minimum number of points ( $MinPts$ )<sup>4</sup>. Ankerst et al. (1999) defines as *directly density-reachable* with respect to  $o$  every point inside  $\epsilon$  and *density-reachable* every point in the transitive hull of direct density reachability limited by the  $MinPts$  parameter, i.e., a point is density-reachable if its directly density-reachable from another directly density-reachable point from  $o$  and so on, where the  $MinPts$  parameter limits that hull. Furthermore, two points  $p$  and  $q$  are density-connected if both are density-reachable from  $o$ . Any two points  $p$  and  $q$  that belong to a cluster must be both density-reachable from  $o$  and density-connected with each other, if not, the points are classified as noise or non-clustered points. OPTICS makes this analysis for each point; identifies the core points and obtains  $\epsilon$  for each point with respect to the nearest core points making it possible to order the data according to this. The information about the density structure of the data is then contained in the Order vs  $\epsilon$  space. Although OPTICS does not consider uncertainties in its procedure, it is useful to consider the order of magnitude of the typical uncertainty in the  $\epsilon$  space and compare with the  $\epsilon$  values in the R plot to place a quantitative criteria for the statistical significance of the cluster retrieved. We consider this together with the results from the Kinematic Analysis to choose the  $\epsilon$  space to be the Galactic Heliocentric Coordinates (X,Y,Z). Then, when applied to the (X,Y,Z) space, OPTICS yields information about the spatial structure of the region and the potential clusters, if any, which can be extracted from the R plot.

#### 3.2.2 The Reachability Plot

The R plot shows the *order* vs  $\epsilon$  space and can be interpreted as follows: clusters can be identified as valleys, and a lower  $\epsilon$  for the core points suggest a more dense cluster. The size of the cluster (number of sources) is identified with the size in the *order* dimension. Even though the global structure of the R Plot is rather insensitive to the input parameters (see Ankerst et al. (1999), Section 4.1), its local shape has dependency on certain parameters; as the number of density-reachable points is proportional to  $MinPts$ , a large value will soften the curve because more points will be classified as part of a cluster. On the contrary, a low value will produce spurious results, i.e., clusters with size smaller than it is possible to resolve with the data given the typical uncertainty, and will classify as noise points that could be part of substructure. A broad range of  $MinPts$  can be

chosen without changing the global structure seen in the R Plot and an optimal value can be chosen via heuristic methods or simple inspection, with minimum effects on the cluster identification. Even though the interpretation of the R plot is very straightforward, the selection of the boundaries of a cluster is still rather subjective. The limits, while not the shape of the plot, depend on the  $\xi$  parameter, which defines the steepness at which the cluster starts and ends with and is set depending of the resolution required. Lower values of  $\xi$  extract broader structures while higher values restrict the cluster classification to higher steepness in the cluster limits. That is, given a local valley in the R plot, the higher we choose  $\xi$  the more conservative we are about the accepted gradient of  $\epsilon$  with respect to *order* at the limit of the valley.

### 3.3 Time Analysis

In this section we describe how we estimate the number of supernovae (SNe) events occurred for a given substructure. In order to do this, we adopt the Kroupa (2001) canonical initial mass function (IMF) and the stellar evolution grids with rotation from Ekström et al. (2012). The IMF has the form

$$\frac{dN}{dM} = k \cdot M^{-\Gamma} \quad (8)$$

Where  $N$  is the number of stars or systems,  $M$  the respective mass and  $\Gamma = 2.3$ . The normalization constant  $k$  is obtained with:

$$k = \frac{N}{\int_{M_{low}}^{M_{up}} M^{-\Gamma} dM} \quad (9)$$

Where  $M_{low}$  is the lower bound in the range of masses spanned by the Turn-Off sample, i.e., approximately the mass of a B2 star, which we assign to be  $7.3 M_{\odot}$ , based on the color-mass estimates from Pecaut & Mamajek (2013) and the measured mass of  $\beta^2$  Sco<sub>\*</sub> of  $7.3 \pm 1 M_{\odot}$ . Since we expect the minimum mass of supernovae progenitors to be  $\sim 8 M_{\odot}$  (Barrientos & Chanamé 2021), integration in the mass range covered by the Turn-off sample should include all of these progenitors present in USco.  $M_{up}$  is the mass of the most massive member in the given stellar population. Assuming that a well behaved function describes the mass-lifetime relation for H and He-burning stages, we estimate the stellar upper mass,  $H-M_{up}$  and  $He-M_{up}$ , at a given age of the parent structure by fitting a spline function (Spl) to this relation from Ekström et al. (2012). This way, we are able to compare the available mass measurements of the most massive stars with the predicted upper limit for the structure they belong to. Furthermore, with this fit we are able to obtain the progenitor's mass  $M_{\tau}$  of a SN event occurred  $\tau$  Myr ago (this is  $He-M_{up}(\tau)$ ), by obtaining the roots of the Spl via the Newton method. We do not consider pre-MS times for this massive stars nor C-burning or latter stages, as they are at least 2 and 3 orders of magnitude lower than the H and He-burning stages, respectively (Siess et al. 2000; Ekström et al. 2012). The number of SN events ( $N_{SN}$ ) that took place within a stellar population  $\tau$  Myr ago is:

$$N_{SN} = \int_{M_{low}}^{M_{\tau}} k \cdot M^{-\Gamma} dM \quad (10)$$

$N_{SN}$  depends on  $N$ ,  $M_{up}$  and  $M_{\tau}$ . When performing this Analysis, we will show that  $N$  is sufficiently well constrained. In several cases the observed  $M_{up}$  values lack precision such that no conclusions could be drawn if only relying on them, however, we also show that approximations can be made to obtain results with statistical relevance and high certainty. Uncertainty in  $M_{\tau}$  directly depends on the

<sup>4</sup> Note that core points are not necessarily unique.



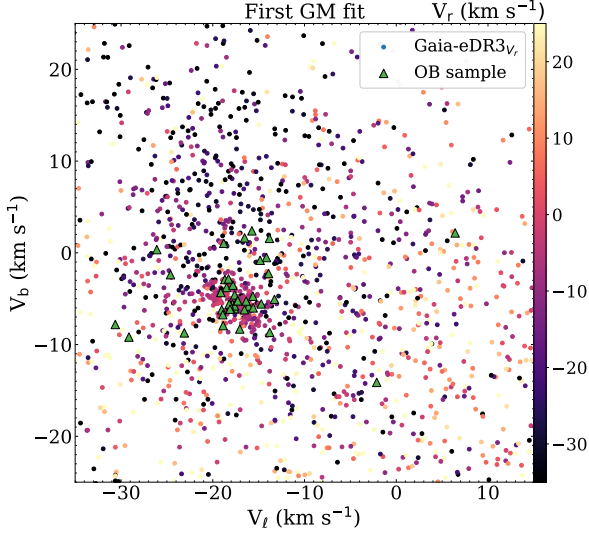


**Figure 1.**  $V_T$  space for the Gaia-eDR3 $_{V_r}$  Sample, where the first GM fit is performed and the OB stars sample. Each cross denote the mean values of a component produced by the GM fit in the  $(U,V,W)$  space. Information about  $V_r$  can be extracted from the color map, the min and max color is assigned to sources outside the color bar's interval. The over density of OB stars gives important information of both the presence and kinematic properties of USco as an OB association. The barycenter motion of USco is chosen as the mean position in the  $(U,V,W)$  space of the GM component that better overlaps with the OB stars in the  $V_T$  space.

model that we are assuming. Additionally,  $N_{SN}$  will also systematically depend on the age of the stellar population under analysis, hence, we report and consider the values related to the upper and lower bounds of the ages estimated for each of the substructures.

## 4 RESULTS

### 4.1 New members in USco

Following the Kinematic Analysis, we recuperate 0 O stars and 31 B stars from Gontcharov (2012) in the Raw Gaia-eDR3 set. We also obtained 17 photometric B stars in the Raw Gaia-eDR3 sample and by doing a crossmatch with the 2MASS catalog with a nearest-neighbor crossmatch with radius of 1 arcsec, we retrieved 23 B stars. After dealing with duplicates, we compile a set of 52 OB stars. We compared the latter sample with the Turn-Off sample (see Sec. 2.2) and found that  $\nu$  Sco $_{\star}$ ,  $\beta^2$  Sco $_{\star}$ ,  $\omega^1$  Sco $_{\star}$ ,  $\pi$  Sco $_{\star}$ , 1 Sco $_{\star}$ , 13 Sco $_{\star}$  and  $\rho$  Sco $_{\star}$  are contained in our OB sample;  $\tau$  Sco $_{\star}$ ,  $\sigma$  Sco $_{\star}$  and  $\beta^1$  Sco $_{\star}$  have no  $\varpi$  measurements in Gaia and  $\delta$  Sco $_{\star}$  and  $\alpha$  Sco $_{\star}$  have no Gaia counterpart. We add the 5 missing stars from the Turn-Off sample to the OB sample<sup>5</sup>, and obtain a total of 57 OB stars. Finally, we double check with Skiff (2009) and discard 9 sources as A stars. The final OB sample contains 47 stars. For  $\sigma$  Sco $_{\star}$ ,  $\beta^1$  Sco $_{\star}$ ,  $\delta$  Sco $_{\star}$  and  $\alpha$  Sco $_{\star}$  we use astrometry from Hipparcos (van Leeuwen 2007).

We applied the GM fit<sup>6</sup> to the Gaia-eDR3 $_{V_r}$  sample in the

$(U,V,W)$  space, this yielded an optimal 3-component mixture, according to the BIC (see Appendix B). Figure 1 shows the positions in the  $V_T$  plane in Galactic coordinates (as none or only a few sources have  $V_r$  in Gaia) for the Gaia-eDR3 $_{V_r}$  sample, the OB sample and the 4 nearest component means to the OB stars, naturally, our selected component is the one with mean  $(V_l \sim -17.3, V_b \sim -5.4)$  km s $^{-1}$ . Hence, we define  $(U_0 = -5.5 \pm 2.7, V_0 = -16.8 \pm 1.7, W_0 = -6.6 \pm 1.9)$  km s $^{-1}$  as the true barycenter motion  $(U, V, W)_{bar}$  of USco, which is consistent with previous estimates from Gaia-DR2 (e.g.  $U, V, W \sim -5, -16, -7$  km s $^{-1}$  by Luhman et al. (2018)) and Gaia-DR1 (e.g.  $U, V, W \sim -6.16, -16.89, -7.05$  km s $^{-1}$  by Wright & Mamajek (2018)). From the obtained  $(U, V, W)_{bar}$ , we calculate  $V_{T*}$  for each source in the Gaia-eDR3 set. We applied a Second GM fit in the  $(V_{T*})$  space for the Gaia-eDR3 set (left panel in Figure 2) and selected 4 as the optimal component number according to the BIC. In this space, the component selected is the nearest one to  $(V_{T*}) = (0, 0)$  km s $^{-1}$  and we chose a confidence region of  $3\sigma$  (3004 sources) from this component as our USco KG (see Section 3.1). The USco KG represents the entire census of USco and is shown in the right panel of Figure 2. The estimated contamination in the USco KG is  $\sim 6\%$  according to Eq.(7).

We perform the analog procedure for the Raw Gaia-eDR3 set based on the OB sample already described. The retrieved sample is composed by 3661 sources with estimated contamination extent  $\sim 9\%$  according to Eq.(7). We found that applying at this point the cuts in Eqs. 4, 5 to the this sample, produces roughly the same data set as the USco KG extracted from the Gaia-eDR3 set.

#### 4.1.1 Hints of older populations

Some B stars in Figure 1 seem to be associated with a broader apparent over density of negative radial velocity sources. As counterpart, left panel of Figure 2 shows two out of four components yielded by the second GM fit (other two fall outside the limits of the figure), as discussed, one of the components is related to USco, but the other component of the second GM fit with its mean centered about  $V_l - V_{l,exp} \sim -2, V_b - V_{b,exp} \sim 6$  km s $^{-1}$  is also related to a notable over density of B stars. A possible explanation for this over densities and their B star counterparts, could be the presence of an older population of stars with barely recognizable kinematic properties. For older populations, we expect their kinematic coordinates to spread, and migrate to merge with those of the Galactic field, making it hard to clearly distinguish them from it. This is consistent with the position and qualitative properties of this component of the second GM fit, however, an in depth analysis of this result is beyond the scope of this work. On the other hand, we do not found potential physical relevance in any other component extracted from the First or Second GM fits.

#### 4.1.2 Membership validation

We compile a set of USco members based on the previous census on Sco-Cen by Damiani et al. (2019); Luhman (2022). These census rely on different selection criteria, data releases from Gaia and report the most detailed characterization of USco with the Gaia data, providing together an ideal sample to validate the membership of the Raw USco KG. After extracting duplicates we obtain 3811 sources. We compare our census with the latter sample. This implies that 338 new sources, with respect to these works, are contained in our work. However, CMD positions for this members suggest they are most likely contamination, coinciding with the percentage estimated in Section 4.1.

<sup>5</sup> Note that  $\alpha$  Sco $_{\star}$  is actually an evolved M type star.

<sup>6</sup> Each GM fit performed in this work converged with a threshold of at least 0.001 km s $^{-1}$

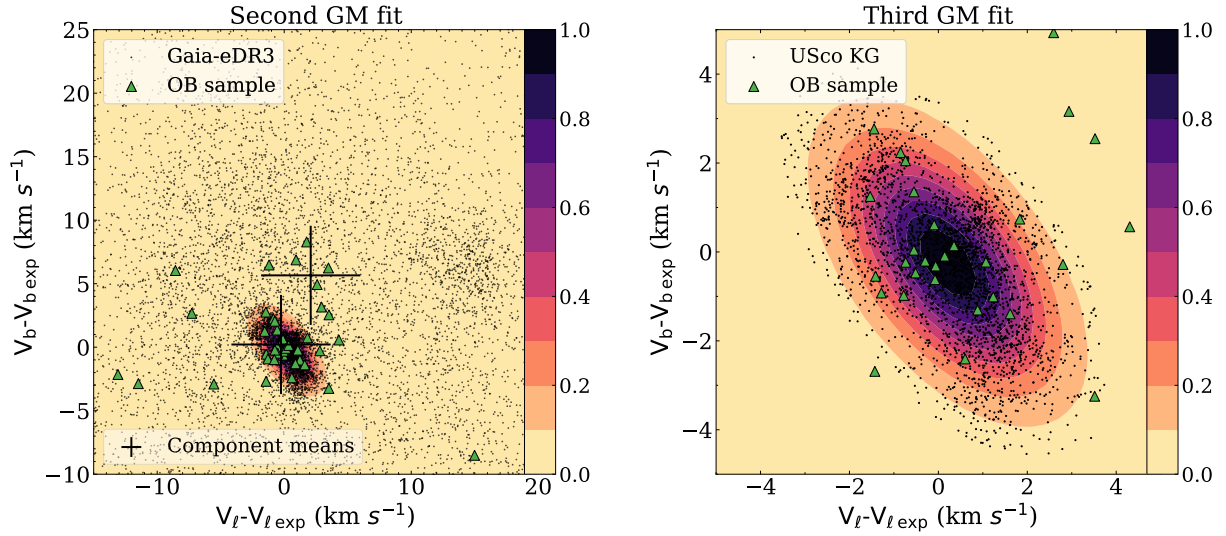


**Figure 2.** Left:  $V_T^*$  space for the Gaia-eDR3 set. Here the USco’s kinematic structure appears as a notorious over density near the origin. The USco KG is composed by the sources within the  $3\sigma$  regime of the component associated with this over density. The BIC suggest 4 components to fit the Gaia-eDR3 set. One of this components is related to the Galactic field stars (around  $\sim 15, \sim 7 \text{ km s}^{-1}$ ). Right:  $V_T^*$  for the USco KG. In the Third GM fit, the BIC is minimized if 3 components are chosen, suggesting the presence of 3 main distinct KGs in USco.  $V_T^*$  space is estimated based on the  $(U, V, W)_{bar}$  values obtained in the First GM. The color map shows the posterior probability (min-max normalized) produced by the GM fit from the Gaia-eDR3 set and the USco KG in the Second and Third GM fit respectively.

#### 4.1.3 Binaries

We note that the large majority of the inferior quality sources in the Raw USco KG are classified as such due to the RUWE threshold in Eq. (5), which is known to be related with unresolved pairs (Lindgren et al. 2021). We further investigate this by comparing the Raw USco KG and the USco KG samples in the CMD and the `ipd_gof_harmonic_amplitude` and `ipd_frac_multi_peak` parameters, where the latter two yield information about the partially resolved and resolved binaries, respectively (Lindgren et al. 2021).

In the left panel of Figure 3 we show the CMD for the Raw USco KG (black) and USco KG (red) with a 10 Myr PARSEC isochrone. We note from Figure 3 that about half ( $\sim 500$ ) of these inferior quality sources have pre-MS positions in the CMD, and hence are true USco members, however, their astrometric quality is diminished as they are probably unresolved, partially resolved or very close binaries. We further support the latter on their trend to have high values of the `ipd_gof_harmonic_amplitude` and `ipd_frac_multi_peak` parameters, which are related to partially resolved and close resolved binaries respectively (Lindgren et al. 2021). The presence of this large fraction of close binaries may yield important information on the dynamics of USco, but a further investigation on the properties of these sources escapes the aims of this work.

## 4.2 Main Kinematic Groups

As very local over densities may have been missed by the global Second GM fit applied on the Gaia-eDR3 set (see Section 3.1), we perform a Third GM fit but on the USco KG (right panel in Figure 2). The Third GM fit produces a minimized BIC if 3 components are chosen (see Figure B1), suggesting that USco is actually composed by at least 3 kinematic substructures. We rule out that uncertainties significantly affect this result because typical propagation errors in

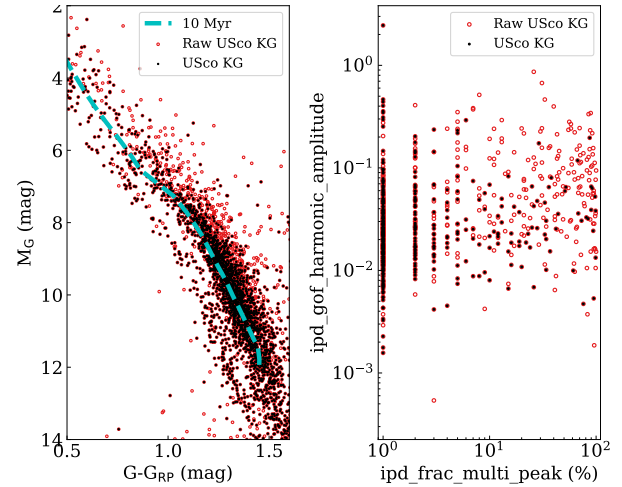


**Figure 3.** CMD with a 10 Myr isochrone (left) and `ipd_frac_multi_peak` vs `ipd_gof_harmonic_amplitude` Gaia parameters for the Raw USco KG and the USco KG. Black dots are the inferior quality sources the where left out from the USco KG mostly due to the RUWE criterion, which is well known to account for unresolved pairs (Lindgren et al. 2021). About half ( $\sim 500$ ) of this inferior quality sources have photometry consistent with being pre-MS stars. These inferior quality sources also tend to have high values of `ipd_frac_multi_peak` and `ipd_gof_harmonic_amplitude`, which are sensitive to resolved and partially resolved binaries respectively (Lindgren et al. 2021).

$V_\alpha$  and  $V_\delta$  are  $\sim 0.1$  and  $\sim 0.2 \text{ km s}^{-1}$ , one order of magnitude lower than the  $1\sigma$  regime of the narrowest  $P(KG_i|V_T^*)$  distribution ( $\sim 2.8 \text{ km s}^{-1}$ ) (see Section 3.1.1). In the following, we assess the physical relevance of the retrieved KGs and the limitations of this method. Figure 2, summarizes the results from the Second and Third GM fits, i.e., left panel shows the Gaia-eDR3 set and the USco KG

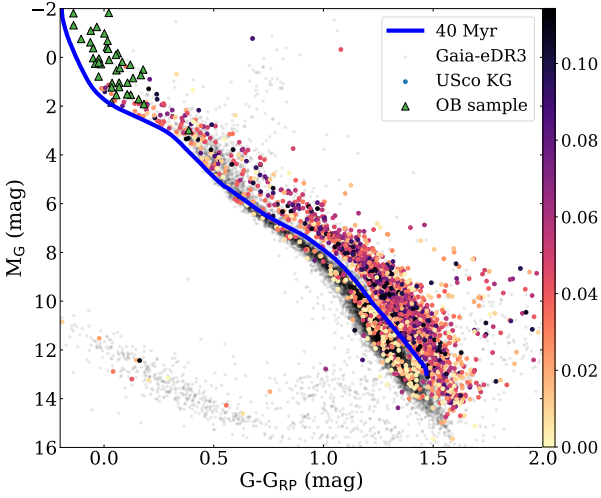


**Figure 4.** Color index  $G-Grp$  vs absolute  $G$  magnitude for the Gaia-eDR3 set and the USco KG. The color map informs about the estimated posterior probability for each star to belong to the USco KG, the same as right panel in Figure 2. A 40 Myr PARSEC isochrone divides the young low-mass pre-MS sources of USco from the MS stars of the Galactic field stars. The 47 stars with Gaia measurements from the OB sample are plotted as blue triangles.

with the respective posterior probabilities (min-max normalized) extracted from the GM fits. We will refer to the 3 KGs retrieved as  $\rho$  Oph KG, USco Young KG and USco Old KG. The  $\rho$  Oph KG is mainly associated with the well known  $\rho$  Ophiuchi region, the USco Young KG contains what typically has been taken as the remaining populations of USco and we present the USco Old KG as a new KG which remains unstudied as such. We will show that the inclusion of the USco Old KG is necessary to understand many important properties of USco. These KGs have mean velocities  $(U, V, W) = (-0.22 \pm 3.6, -16.2 \pm 0.7, -6.7 \pm 1.8)$ ,  $(-1.3 \pm 3.6, -17.0 \pm 0.9, -5.1 \pm 1.7)$ ,  $(-2.6 \pm 7.3, -18.8 \pm 0.9, -4.0 \pm 2.2)$  km s<sup>-1</sup>, for the  $\rho$  Oph, USco Young and USco Old KGs, respectively.

In Figure 4 we show the  $G-Grp$  vs  $M_G$  CMD for both the Gaia-eDR3 set and the USco KG. The color map indicates the posterior probability for each source to belong to the USco KG. A 40 Myr PARSEC (Bressan et al. 2012; Chen et al. 2014; Marigo et al. 2017) isochrone is plotted to illustrate the division between the USco members from the Galactic field stars, from this, we note that low probability sources are also very likely to belong to the Galactic field populations, but also to the young stellar objects commonly associated with the  $\rho$  Oph complex. Table 1 show the estimates of the mixing percentiles for each KG, including USco (see Section 3.1.1). Rows show the USco KG and the remaining kinematic substructures in the confidence intervals selected, while columns indicate how many stars from a given KG are expected to be in the given confidence intervals for each row.

The Figure 5 shows the sources with  $P(KG|V_{T*}) > 50\%$  for each KG<sup>7</sup> described by the color map. 644, 702 and 467 sources are retrieved for the  $\rho$  Oph, USco Young and USco Old KGs respectively. The USco KG is shown as gray background such that for each KG in USco (columns) a direct comparison on the parameters (rows) can

Kinematic Group	$\Sigma P(\rho V_{T*})$	$\Sigma P(Young V_{T*})$	$\Sigma P(Old V_{T*})$
USco	35.6 %	36.8 %	27.6 %
$\rho$ Oph	–	8.2 %	0.2 %
USco Young	14.9 %	–	9.1 %
USco Old	0.2 %	4.4 %	–

**Table 1.** Rows: USco KG and the KGs retrieved with the Third GM fit with  $P(KG_i|V_{T*}) > 50\%$  (min-max normalized). Columns:  $\%_{mix}$  for each KG in the given regions.

be made. The first and second rows show the  $V_{T*}$  space, where the fit was made, and the observed proper motion, respectively. The third row shows the  $V_r$  histogram with the 36 ( $\rho$  KG), 49 (USco Young KG) and 44 (USco Old KG) sources with available  $V_r$  measurements in the interval  $[-15, 5]$  km s<sup>-1</sup>, the means for the sources in the entire range is  $(-8.1, -3.9, -2.8)$  km s<sup>-1</sup> suggesting that the groups are also separated in this directly observed space, however, the typical error in  $V_r$  for the entire USco KG is  $\sim 2.79$  km s<sup>-1</sup> and we can not rule out field star contamination or the intrinsic internal mixing between groups as the cause of this separation. The last row shows the CMD for the absolute  $G$  magnitude ( $M_G$ ) and color index  $G-Grp$  for the three KGs, each with a 10 Myr PARSEC isochrone for a relative age comparison between the groups. This CMDs suggest an age gradient between the groups. Note that the extinction vector is  $\sim$  parallel to the isochrones in the color range shown, hence, extinction affected sources are displaced approximately along the isochrones implying that ages inferred from this CMD are confident enough to at least extract information of the relative ages of these stellar populations. The overall kinematic properties suggest a true physical distinction between the  $\rho$  Oph, USco Young and USco Old KGs and from this CMDs we infer an unambiguous age distinction between the  $\rho$  Oph and USco Old groups, this is consistent with the results from the kinematic spaces and serves as an independent confirmation of  $\rho$  Oph KG and USco Old KG as distinct physical groups. Besides, supports the conclusion that the kinematic mixing between the USco Young KG and the other populations is non-negligible. Furthermore, the first row in Figure 6 shows a double peaked distance distribution for each KG. As the typical propagation error is  $\sim 2$  pc ( $< 3$  pc for  $\sim 80\%$  of the sources), the 2 peaks for the KGs are likely to be real. The rows below, which are projections in the  $(Y, X)$ ,  $(X, Z)$  and  $(Y, Z)$  Galactic sub-spaces, help to clarify this; for the  $\rho$  Oph KG, at least 3 rather compact substructures are revealed  $(X, Y, Z \sim (132, -18, 42), (128, -12, 55), (140, -17, 60)$  pc), mainly, in the  $(X, Z)$  and  $(Y, Z)$  projections, 2 of them explain the distance peak at 140 pc ( $X \sim 130$  pc). In the case of the USco Young KG, 2 rather definite substructures appear at  $(X, Y, Z \sim (130, -22, 55), (128, -15, 43)$  pc) and a third diffuse covering the region ( $X > 135$  pc,  $Y < -19$  pc,  $Z < 52$  pc). Finally, the USco Old KG is mainly constituted by 1 small apparent substructure  $(X, Y, Z \sim (100, -20, 38)$  pc) and a widely spread Diffuse population towards the east of USco, connecting it with the Upper Centaurus Lupus (UCL) region (see Damiani et al. (2019), its Figure 37).

Analogue procedures to the Kinematic Analysis, have been used as the main tool in recent works (e.g., Luhman et al. 2018; Luhman & Esplin 2020; Luhman 2022) to investigate the kinematic substructure. However, this result suggests that the GM fit does not completely disentangles the spatial or age substructure of USco, i.e., there may be true substructures with too similar kinematics as to be separated via this method.

On the other hand, the USco Old KG has been left out of some

<sup>7</sup>  $P(KG_i|V_{T*})$  is min-max normalized.

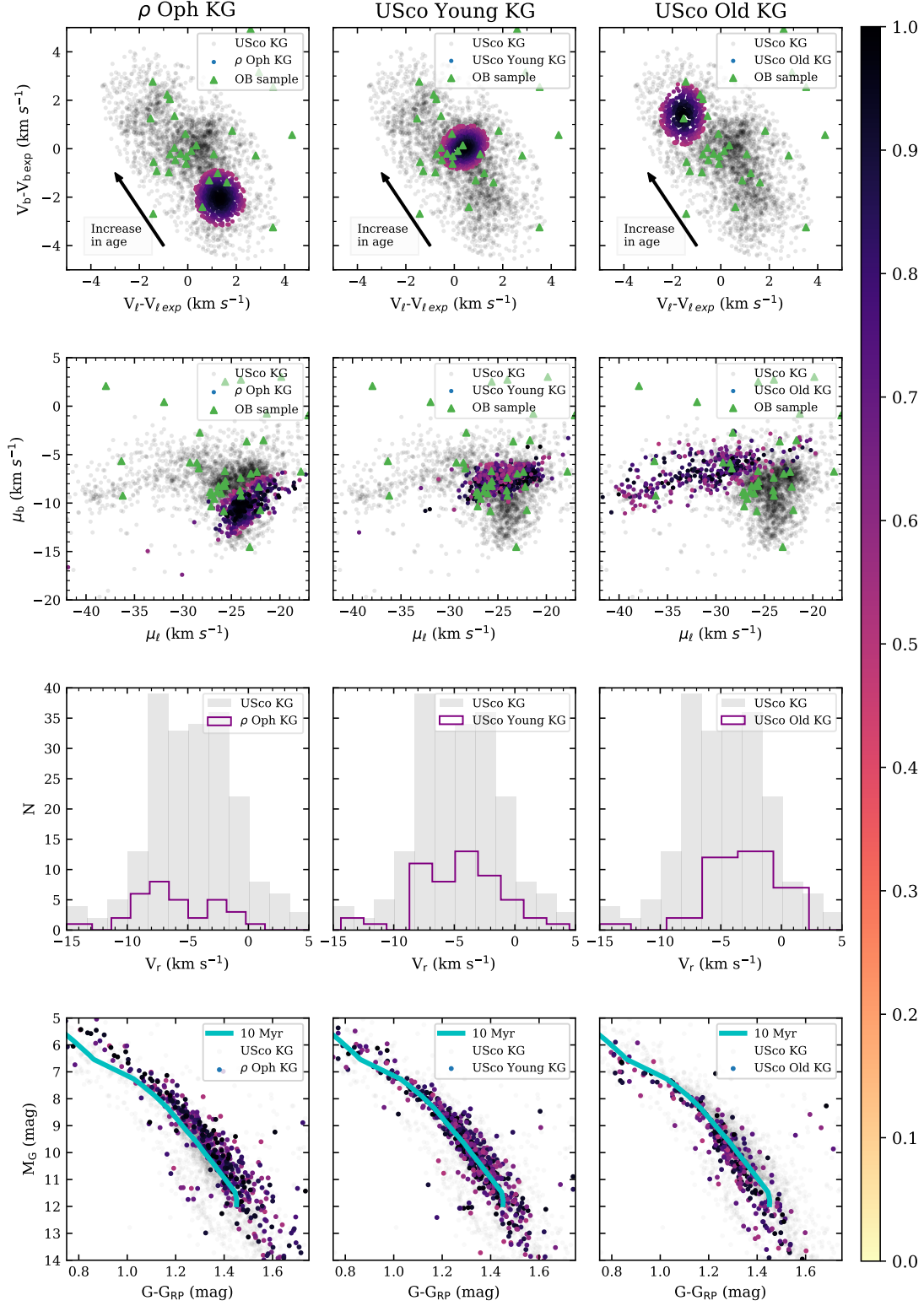


**Figure 5.** Columns: from left to right, the  $\rho$  Oph, USco Young and USco Old KGs. **Rows:** 1st:  $V_T^*$  space. 2nd: proper motion space. 3rd:  $V_r$  distribution. 4th: CMD with a 10 Myr PARSEC isochrone. The color maps the min-max normalized  $P(KG_i | V_T^*)$ . Only sources with  $P(KG_i | V_T^*) > 50\%$  are plotted. The USco KG is shown as the gray background and stars from the OB sample are shown as green triangles. A direct comparison can be done between the different groups and the spaces of interest, revealing a direct relation between position in the kinematic spaces and age.



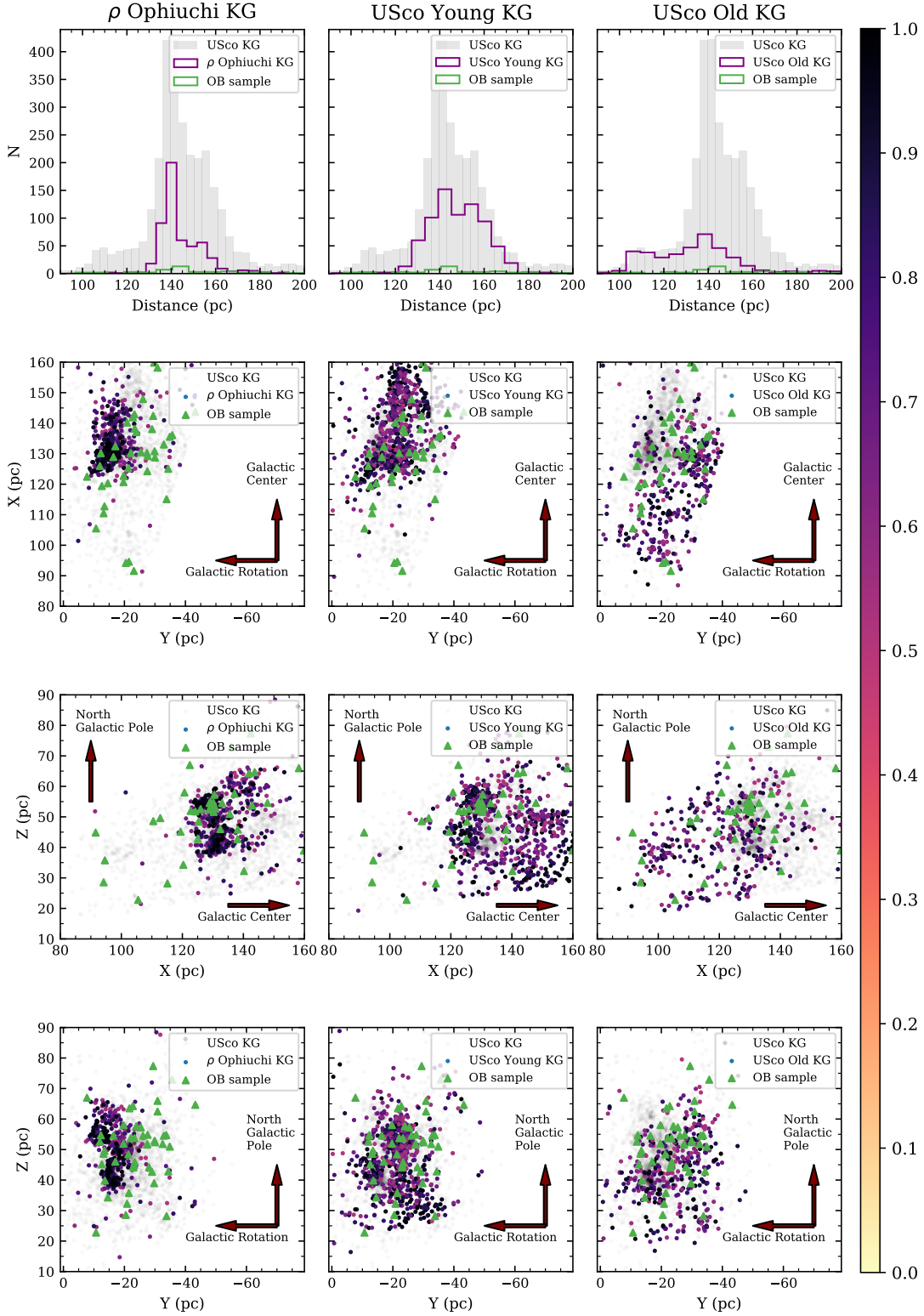


**Figure 6.** Columns: same as Figure 5. Rows: 1st: Distance distribution. 2nd: Projection on the (Y,X) plane. 3rd: Projection on the (X,Z) plane. 4th: Projection on the (Y,Z) plane. Colors: same as Figure 5. The distance distribution for the 3 KGs is double peaked, with all 3 groups showing a peak at  $\sim 140$  pc. Spatial distribution shows a complex structure for each KG, suggesting that clustering in kinematic spaces does not implies spatial clustering in USco and that spatial mixing between this KGs is non-negligible. The selected OB stars mostly overlap with the USco Young and USco Old KGs and tend to be in the external regions of USco.

recent studies on USco based on the Gaia data, for example, the previous works by [Luhman & Esplin \(2020\)](#), [Damiani et al. \(2019\)](#) and [Kerr et al. \(2021\)](#) with Gaia-DR2 data have omitted the inclusion of the USco Old KG mainly due to: 1. They apply clustering techniques like GM but in the proper motion offset space, where uncertainties are lower but, due to its large distance dispersion and lower density, the USco Old KG does not appear clustered, so that on a conservative confidence intervals it may be classified as contamination. This was indeed the case for the analysis of [Luhman & Esplin \(2020\)](#) (see its Figure 6). 2. In the work of [Damiani et al. \(2019\)](#), the selection method produces a rather complete final sample and contains most sources from the USco Old KG, but no systematic way of look for KGs in the  $V_T$  space in USco is performed (see its Figs.12,13,14). 3. The clustering space investigated with HDBSCAN by [Kerr et al. \(2021\)](#) requires both spatial and kinematic clustering, allowing them to recover the substructure SC-13 but as completely separated from USco, when it is probably related to the SC-17-A substructure.

### 4.3 Internal structure of USco

In following sections we show how our OPTICS implementation in the Gaia eDR3 data verifies and significantly complements the previous investigation of the substructure in USco by producing new and more robust results about it.

#### 4.3.1 Spatial distribution

The parameter selection of the OPTICS algorithm largely depends on the intended resolution of the analysis to perform. We limit our analysis to identify spatial substructures in the USco KG, if present, containing at least 31 sources ( $\sim 1\%$  of our USco KG). We explored the ( $MinPts$ ,  $\xi$ ) parameters in the ranges [2,41], [0.006,0.06] and report the results of choosing [ $MinPts = 31$ ,  $\xi = 0.007$ ]. Varying  $MinPts$  from 21 to 41 does not produce any significant change in the global or local shape of the R plot (see Section 3.2.2), values below 21 produce noisy steepness in the already present valleys, which makes difficult to choose  $\xi$  when assigning cluster limits, but the global structure is roughly the same. Values below 21 start to introduce too local valleys with typically  $\sim 10$  sources introducing noise and smaller substructures. The structure most affected by this changes is the labeled as UCL's for its spatial position, as it disappears and strongly changes its shape when varying this parameter, hence, we omit its inclusion as a well defined structure and also any further analysis of it. As  $MinPts$  only needs to be large enough to distinguish the substructures with the intended resolution ([Ankerst et al. 1999](#)), we chose  $MinPts = 31$  and discarded the analysis of  $MinPts > 41$ . Once the  $MinPts$  is set, we start to vary  $\xi$  from 0 to the maximum value where all the valleys with at least 31 sources are selected as clusters ( $\xi = 0.005$ ) in 0.001 steps. Our main analysis is based on  $\xi = 0.007$  as it is the first non-trivial value for  $\xi$ , given  $MinPts$ , we also study the effects of varying  $\xi$  from 0.007 until the point where none of the valleys are selected as a substructure ( $\xi = 0.06$ ).

The R plot (see Section 3.2.2) produced by OPTICS is shown in the top panel of Figure 7. Each source has a position in the R plot and each substructure satisfying the conditions above mentioned is shown in a different color, while the Diffuse populations in USco are identified with black dots. In Figure 7 we show the direct imprint of the spatial structure of USco and evidence for the presence of 8 substructures plus the Diffuse populations, where a total of 1049 and 2065 sources belong to the clustered and Diffuse populations,

**Table 2.** Candidate members of the Upper Scorpius Kinematic Group.

Column Label	Description
source_id	
ra	Right ascension from Gaia eDR3
ra_error	Error in ra from Gaia eDR3
dec	Declination from from Gaia eDR3
dec_error	Error in dec from Gaia eDR3
parallax	Parallax from Gaia eDR3
parallax_error	Error in parallax from Gaia eDR3
distance	Distance by inversion of parallax
pmra	Proper motion in ra from Gaia eDR3
pmra_error	Error in pmra from Gaia eDR3
pmdec	Proper motion in dec from Gaia eDR3
pmdec_error	Error in pmdec from Gaia eDR3
ipd_gof_harmonic_amplitude	Amplitude of the Image Parameter Determination Goodness of Fit versus position angle of scan
ipd_frac_multi_peak	Percent of successful-Image Parameter Determination windows with more than one peak
ruwe	Renormalized unit weight error from Gaia eDR3
phot_g_mean_mag	Magnitude in the G band from Gaia eDR3
phot_rp_mean_mag	Magnitude in the $G_{RP}$ band from Gaia eDR3
M_g	Absolute magnitude in the G band
dr2_radial_velocity	Radial velocity from Gaia DR2
dr2_radial_velocity_error	Error in radial velocity from Gaia DR2
l	Galactic longitude
b	Galactic latitude
pml	Proper motion in the $\ell$ direction
pmb	Proper motion in the $b$ direction
vl	Tangential velocity in the $\ell$ direction
vb	Tangential velocity in the $b$ coordinate
vl_exp	Expected tangential velocity in the $\ell$ direction
vb_exp	Expected tangential velocity in the $b$ direction
X	Cartesian heliocentric coordinate in the direction of the Galactic center
Y	Cartesian heliocentric coordinate in the direction of the Galactic rotation
Z	Cartesian heliocentric coordinate in the direction of the North Galactic Pole
p_rho_Oph_kg	$\rho$ Ophiuchi KG posterior probability from the third GM fit
p_usco_young_kg	USco Young KG posterior probability from the third GM fit
p_usco_old_kg	USco Old KG posterior probability from the third GM fit
epsilon	$\epsilon$ value yielded by OPTICS
V_core	$V_{core}$ from Equation 12
substructure	Label assigned by OPTICS

Labels assigned by OPTICS: -1: Diffuse populations, 0:  $\pi$  Sco, 1:  $\rho$  Oph, 2:  $\omega$  Sco, 3:  $\nu$  Sco, 4:  $\delta$  Sco, 5:  $\alpha$  Sco, 6:  $\beta$  Sco, 7: UCLs. Data from this table will be provided as supplementary material to this paper.

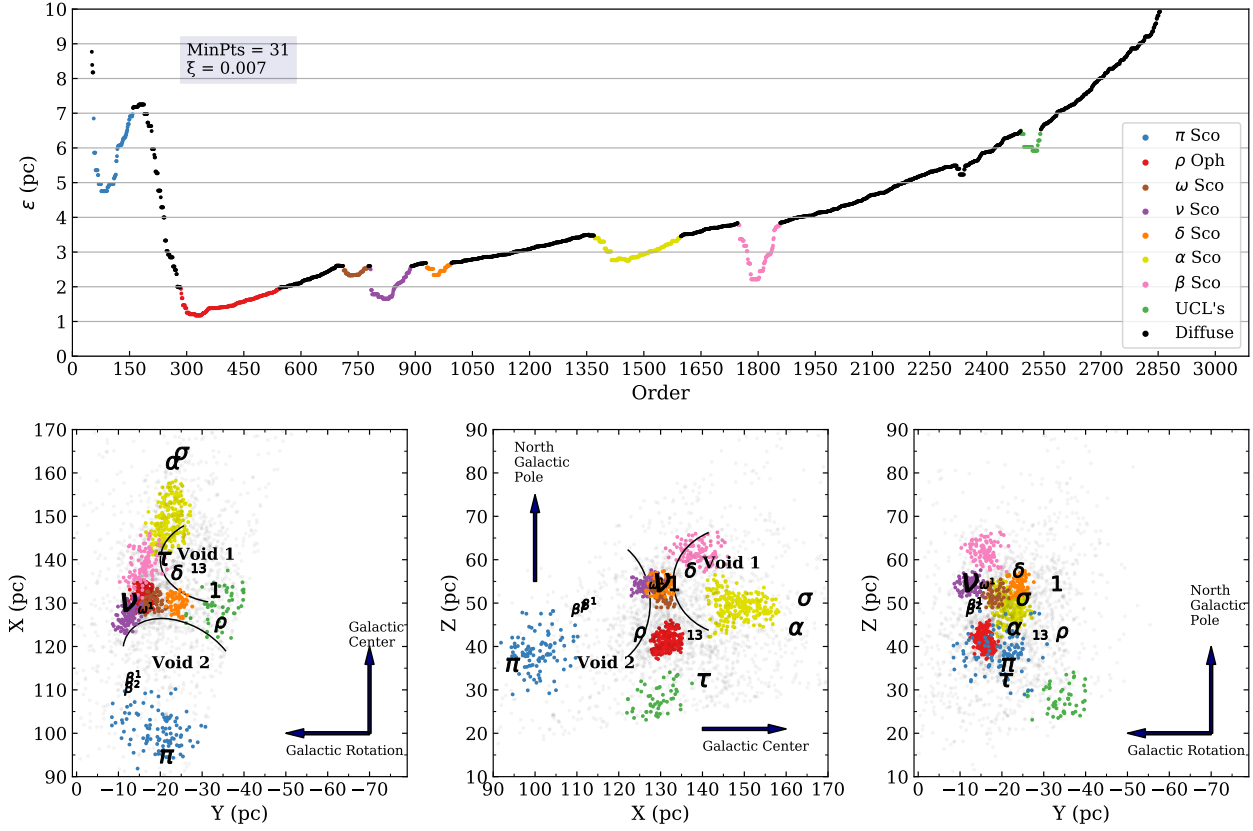


**Figure 7.** Top: R plot for the USco KG with  $MinPts=31$  and  $\xi=0.007$ . Colored valleys represent each structure classified as a cluster in (X,Y,Z) space by the OPTICS algorithm with the given parameters. Diffuse populations are identified as black plateaus. Bottom: from left to right, projections on the Galactic (Y,X), (X,Z) and (Y,Z) planes. Colors represent each substructure extracted from the R plot. The Diffuse populations are plotted in gray. The stellar voids observed are shown as elliptical arcs where such geometry can be clearly assigned. The position of stars from the Turn-off sample is represented by the respective Bayer designation. Note that the Turn-off sample does not include the star  $\rho$  Ophiuchi, hence, the  $\rho$  symbol in this and the following figures corresponds to the star  $\rho$  Scorpii.

Substructure	$\rho$ Oph	$\alpha$ Sco	$\beta$ Sco	$\pi$ Sco	$\nu$ Sco	$\omega$ Sco	$\delta$ Sco	Diffuse
$N_*$	261	227	111	104	108	66	66	2009
$N_{V_r}$	16	14	4	15	7	4	7	188
$N_{A_G}$	47	165	106	20	103	59	59	835
$\alpha$ [deg]	$246.4 \pm 0.6$	$244.5 \pm 1.0$	$241.3 \pm 0.8$	$240.7 \pm 2.7$	$242.7 \pm 0.5$	$242.1 \pm 0.8$	$239.8 \pm 0.7$	$243.6 \pm 4.6$
$\delta$ [deg]	$-24.1 \pm 0.7$	$-24.6 \pm 1.1$	$-19.5 \pm 0.9$	$-24.5 \pm 2.3$	$-19.4 \pm 0.6$	$-21.9 \pm 0.7$	$-23.1 \pm 0.6$	$-24.6 \pm 3.8$
$\varphi$ [mas]	$7.2 \pm 0.1$	$6.3 \pm 0.2$	$6.5 \pm 0.1$	$9.1 \pm 0.3$	$7.2 \pm 0.1$	$7.1 \pm 0.05$	$7.0 \pm 0.1$	$7.2 \pm 1.8$
$d$ [pc]	$138.7 \pm 2.0$	$158.2 \pm 4.1$	$152.8 \pm 3.0$	$109.9 \pm 4.3$	$138.8 \pm 2.1$	$141.4 \pm 1.1$	$143.0 \pm 1.7$	$144.2 \pm 21.4$
$X$ [pc]	$131.4 \pm 1.8$	$148.7 \pm 4.3$	$138.8 \pm 3.2$	$101.0 \pm 4.3$	$127.2 \pm 2.0$	$130.1 \pm 1.4$	$130.0 \pm 1.7$	$134.2 \pm 20.3$
$Y$ [pc]	$-15.8 \pm 1.2$	$-22.0 \pm 2.3$	$-16.0 \pm 2.1$	$-19.4 \pm 5.0$	$-12.4 \pm 1.5$	$-18.2 \pm 1.5$	$-24.1 \pm 1.3$	$-21.7 \pm 9.3$
$Z$ [pc]	$41.1 \pm 1.8$	$49.4 \pm 2.8$	$61.7 \pm 2.0$	$38.8 \pm 4.1$	$54.2 \pm 1.3$	$52.2 \pm 1.7$	$54.3 \pm 1.6$	$46.2 \pm 12.8$
$\mu_\alpha$ [mas yr $^{-1}$ ]	$-7.6 \pm 2.0$	$-10.3 \pm 1.2$	$-9.8 \pm 1.1$	$-20.3 \pm 2.5$	$-9.2 \pm 1.4$	$-10.4 \pm 1.0$	$-12.6 \pm 1.0$	$-12.2 \pm 4.8$
$\mu_\delta$ [mas yr $^{-1}$ ]	$-25.7 \pm 1.5$	$-21.8 \pm 1.3$	$-21.7 \pm 0.7$	$-31.8 \pm 2.4$	$-24.0 \pm 1.1$	$-24.1 \pm 1.0$	$-24.0 \pm 0.9$	$-24.5 \pm 6.5$
$v_r$ [km s $^{-1}$ ]	$-0.42 \pm 1.8$	$4.8 \pm 18.9$	$-8.8 \pm 4.6$	$-0.2 \pm 2.7$	$-8.0 \pm 1.2$	$-1.9 \pm 7.6$	$-7.0 \pm 1.2$	$-6.5 \pm 17.8$
$U$ [km s $^{-1}$ ]	$-0.1 \pm 1.7$	$3.9 \pm 17.6$	$-7.8 \pm 4.3$	$-2.4 \pm 2.6$	$-6.6 \pm 1.8$	$-1.3 \pm 7.1$	$-7.5 \pm 1.0$	$-7.4 \pm 16.6$
$V$ [km s $^{-1}$ ]	$-16.0 \pm 0.9$	$-18.0 \pm 3.3$	$-15.8 \pm 0.9$	$-19.0 \pm 1.1$	$-15.2 \pm 0.8$	$-16.3 \pm 1.2$	$-16.4 \pm 0.3$	$-16.6 \pm 2.6$
$W$ [km s $^{-1}$ ]	$-7.2 \pm 1.5$	$-3.9 \pm 5.8$	$-8.7 \pm 1.7$	$-4.1 \pm 1.5$	$-8.4 \pm 0.7$	$-6.8 \pm 2.2$	$-7.8 \pm 0.6$	$-7.0 \pm 6.0$
$A_G$ [mag]	$1.7 \pm 0.76$	$1.2 \pm 0.94$	$0.51 \pm 0.30$	$0.20 \pm 0.20$	$0.78 \pm 0.58$	$0.55 \pm 0.29$	$0.44 \pm 0.34$	$0.58 \pm 0.62$

**Table 3.** Mean astrometric parameters and extinction in the G band, with  $1\sigma$  standard deviations for the seven substructures of USco and the Diffuse population identified with OPTICS. The number of available sources with radial velocity and extinction values is also listed.

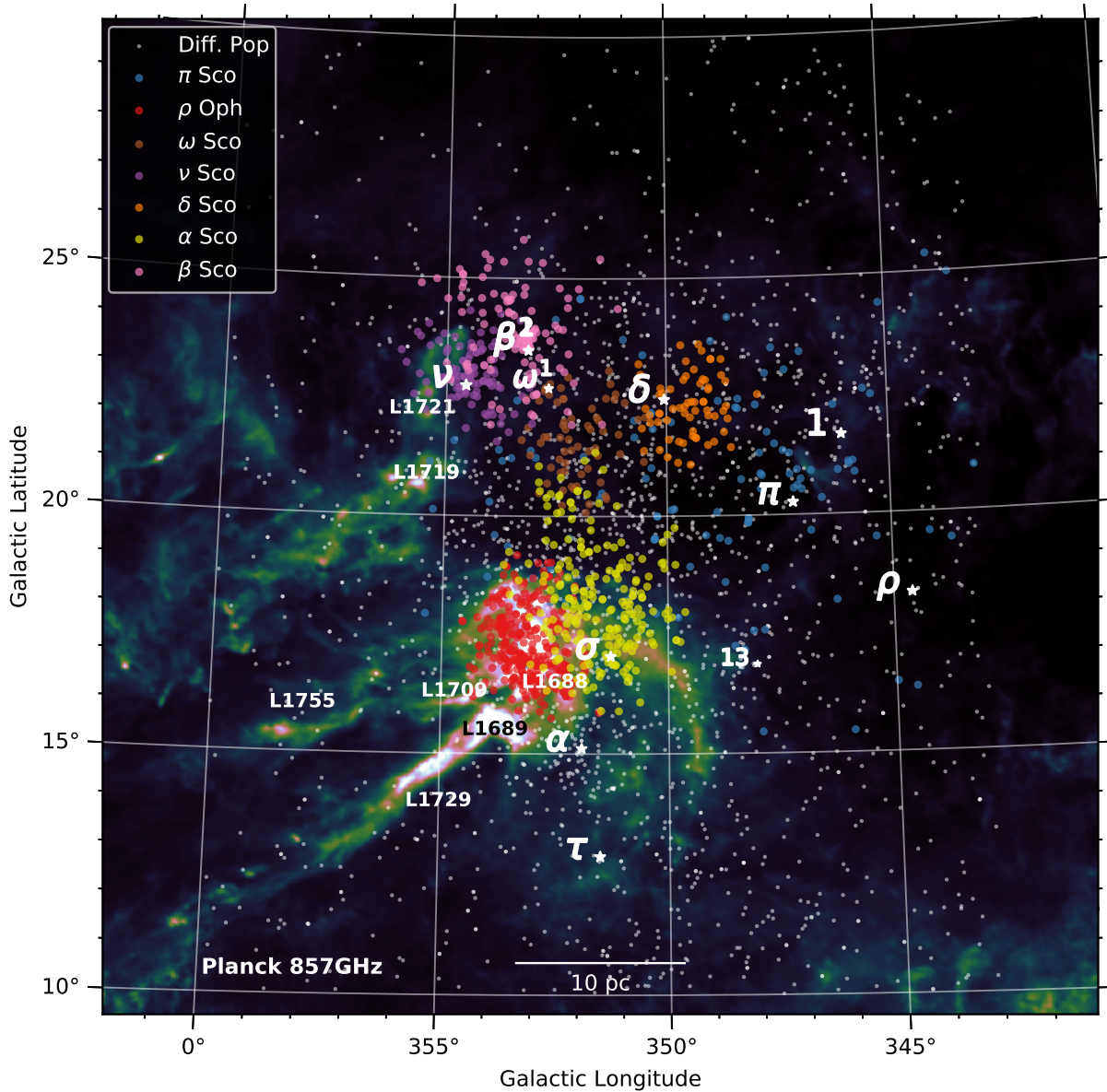


**Figure 8.** Celestial positions in galactic ( $\ell, b$ ) coordinates for each clustered substructure (colors) and the Diffuse populations (light gray) retrieved with OPTICS. The stars of the Turn-off sample are plotted as with star symbols with their Bayer designation at the left. The background is an image from Planck at 857 GHz in the USco region and allows to see the dust emission related to HI structures and molecular clouds. The main Lynds clouds are identified. The scale of 10 pc is at  $d \sim 140$  pc.

respectively. We suggest to name six of these structures after their brightest star (see footnote 1):  $\pi$  Scorpii,  $\omega$  Scorpii,  $\nu$  Scorpii,  $\delta$  Scorpii,  $\alpha$  Scorpii and  $\beta$  Scorpii. The relation between these structures and the respective stars is first shown in this work, and will be discussed in section 4.5. We also recover the well known  $\rho$  Ophiuchi substructure and another minor substructure that we will label UCL's. From the work of Kerr et al. (2021), we recover the substructures SC-13 ( $\pi$  Scorpii), SC-17-E,G,I ( $\nu, \beta$  Scorpii and  $\rho$  Ophiuchi)

and increase their membership in at least 2 and up to 4 times the previous estimates. We find that the substructure H is actually composed by 2 substructures ( $\omega, \delta$  Scorpii). SC-17-B,C,D are largely contained in  $\alpha$  Scorpii substructure. We do not found evidence for the presence of the SC-F substructure and we argue that SC-A is more likely to be a spurious detection and part of the larger  $\pi$  KG. Hence, we introduce 3 new substructures ( $\omega, \delta, \alpha$  Scorpii) plus the physical relation of all the substructures with one of the most mas-



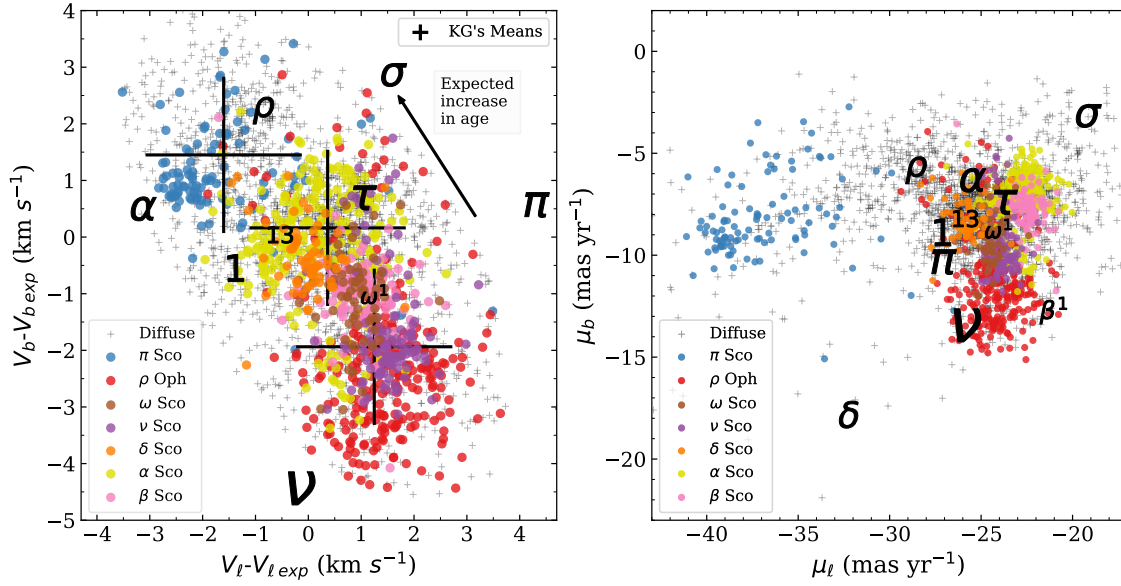


**Figure 9.** Left:  $V_T^*$  space. The 7 substructures retrieved with OPTICS are shown. We plot the expected direction where the age increases and crosses centered on the mean positions of the  $\rho$ ,  $\alpha$  and  $\pi$  KGs, according to the results from the Kinematic Analysis. The crosses have width  $\sim 1\sigma$  of the fitted components. Right: proper motion. Notably, these spatially clustered populations are also highly clustered in these kinematic spaces. Correcting perspective and depth effects is important, as the trend and relative positions of the substructures are better extracted from the  $V_T^*$  space.

sive members in USco. Table 3 shows the mean values of the main astrometric variables for each of the 8 analyzed substructures<sup>8</sup> and their respective  $1\sigma$  standard deviations. The lower panels in Figure 7 show the spatial projections of the five major substructures with  $> 100$  sources, the other two with 66 sources each and the Diffuse populations (gray background) in the Galactic (X,Y,Z) coordinate sub-spaces plus the stars in the Turn-Off sample with white star symbols. Figure 7 show unprecedented insights on the internal structure of USco. Among the most notable characteristics from the spatial distribution of this substructures are the apparent voids shown in the lower panels of Figure 7. These voids are apparently well fitted by ellipsoids connected at their edges (the arcs shown in Y-X and X-Z projections) by the  $\rho$  Oph,  $\beta$  Sco,  $\omega$  Sco,  $\nu$  Sco, and  $\delta$  Sco substructures. We will revisit the relation between the Voids and the substructures when analyzing the star formation history of USco in Section 5.4.

To obtain a quantitative idea of the reliability of these results, we base on the OPTICS'  $\xi$  parameter. When varying the  $\xi$  parameter, we note that each substructure begins to lose members when the gradient of the valley in the R plot is too low with respect to  $\xi$ , this means that changing the  $\xi$  parameter can give us an idea on how definite are the boundaries of a cluster relative to its surroundings. Paradoxically, the first substructure in losing members, at  $\xi = 0.007$ , is the associated with  $\rho$  Oph (red valley in Figure 7), the most deeply studied region in USco. This by itself is evidence of the true physical relevance of the new substructures extracted with OPTICS as they are more robustly clustered than  $\rho$  Ophiuchi. On the other

hand, we note by the same methods that the  $\beta$  Sco and  $\pi$  Sco substructures are the most well defined substructures retrieved, which is also noted from their higher steepness in the R plot. The celestial ( $\ell, b$ ) position of these substructures and the Diffuse populations is shown in Figure 8. A Planck 857 GHz dust emission background is also plotted with visualization purposes; the dust emission maps very well the HI structures at low densities and shows an excess of about 40% with respect to the HI emission in high density regions where molecular clouds are also present (Planck Collaboration et al. 2011), several Lynds clouds are also shown with this purpose. We also mark the positions of the brightest members of USco.

#### 4.3.2 Kinematics

The kinematic properties of this substructures can be seen in Figure 9, where we show the 7 substructures in the  $V_T^*$  (left) and proper motion (right) spaces. We include the Turn-Off sample in this plots, however, this proper motion and parallax measurements have non-negligible errors because they are strongly affected by binary interactions, deviating their kinematics from that of their parent substructures. These shows how the inclusion of transverse velocities would bias and reduce our member selection due to the unresolved binary interactions. Note that several substructures do not overlap with each other within the proper motion space as clearly as they do in the  $V_T^*$  space. In particular, these effects are needed to be taken into consideration for the investigation of the Wall of USco. We also include the direction towards we expect for the age of all the substructures to increase, based on results from section 4.2. In contrast with the results obtained in section 4.2, substructures are compact and well defined in both (X,Y,Z) and  $V_T^*$  spaces. Moreover, substructures are aligned in roughly the same direction the Kinematic Analysis

<sup>8</sup> We omit the analysis of the UCLs substructure (51 sources) because of its noisy character and its truncated position towards the Upper Centaurus Lupus region.

suggests an increase in age with respect to the  $V_{T*}$  space. The 7 substructures constitute four clearly evident sub KGs, where four of them unambiguously overlaps with the high confidence region of the three KGs obtained in the Kinematic Analysis and the remaining two,  $\beta$  and  $\omega$  Sco, are located between two of these KGs, providing a way of testing how intrinsic is the age- $V_{T*}$  dependency suggested by the Kinematic Analysis. We also note that  $\delta$ ,  $\beta$ ,  $\omega$  and  $\nu$  Sco are particularly close in both (X,Y,Z) and  $V_{T*}$  spaces a present a correlated directionality in these spaces. In the following, we try to obtain some insights on the age trend observed in the Kinematic Analysis in terms of substructures discussed.

#### 4.3.3 Ages

Here we make relative and intrinsic estimations for the substructures found in section 4.3. In order to do this, we use PARSEC (Bressan et al. 2012; Chen et al. 2014; Marigo et al. 2017) isochrones and the G,  $G_{RP}$  Gaia-eDR3 passbands, as they exhibit lower extinction and errors than  $G_{BP}$ . We aim to provide an insight into the age properties of this substructures to see if the expected age trend shown in Figure 9 is true for them, which may be tested extracting, if possible, relative ages between them from the CMD. While substructures show clearly distinct relative ages, in most cases, intrinsic age estimations are systematically affected, at least, by extinction effects at the individual level, hence, we include conservative systematic and statistic error estimations for the ages reported. Luhman & Esplin (2020) gives  $A_K$  (Ks passband from 2MASS) estimates for USco sources excluding the  $\rho$  Oph region. Assuming a Cardelli reddening law (Cardelli et al. 1989), we transform  $A_K$  values from Luhman & Esplin (2020) into  $A_G$ . In Figure 10 we show the resulting CMDs with 6, 7, 8, 9, 14 and 20 Myr extinction-corrected isochrones. We assume a solar metallicity of  $Z=0.014$  to be consistent with the grids from Ekström et al. (2012) in the Time Analysis.  $A_G$  mean values for each substructure are shown in Table 3. We take  $A_G=0.6$  when correcting isochrones for  $\delta$  Sco,  $\beta$  Sco,  $\omega$  Sco and  $\nu$  Sco since extinction does not vary significantly from this mean value for these substructures. To estimate intrinsic ages we base on a maximum age of  $\rho$  Oph complex of 5-6 Myr (Cánovas et al. 2019; Esplin & Luhman 2020). The uncertainty in this value systematically propagates to our results. We chose a particular interval to estimate ages as different intervals yield different results. To chose the optimal interval we consider the following: 1. We aim to reproduce the 6 Myr upper age of  $\rho$  Oph substructure. 2. Age estimations based on the region  $G-G_{RP} < 1$  would be strongly affected by low number statistics and unresolved binaries. 3. Current stellar evolutionary models are considered unreliable for late M objects (Pecaut & Mamajek 2016), in particular, observations suggest an underestimation of their radius (e.g., Boyajian et al. 2012), so we want to avoid as many late M stars as possible. By characterizing and constraining the fundamental properties of M stars, Kraus et al. (2011) concluded that M objects with mass  $> 0.35 M_\odot$  should be well described by current models at the time of Version 1.1 of the PARSEC grids, that we use in our work. Consistently, dispersion, deviation and the deviation gradient significantly increase at  $G-G_{RP} > 1.25$ . At this mass regime, pre-MS M sources have an underestimated temperature by  $\sim 100$  K (see Pecaut & Mamajek (2013), tables 5 and 6), hence, we estimate ages based on the  $G-G_{RP}$  interval [1.1,1.25], marked with vertical lines in both panels of Figure 10. This interval would correspond to a mass range of  $\sim [0.27-0.44] M_\odot$  (Pecaut & Mamajek 2013; Luhman 2022). We make age estimations for the remaining substructures relative to these considerations. From left panel in Figure 10 we see that the age trend observed in the Kinematic Analysis (see

Figure 5) holds for these substructures, i.e.,  $\rho$  Oph (6 Myr max),  $\alpha$  Sco (14 Myr) and  $\pi$  Sco (20 Myr), where all of this structures unambiguously belong to one of the KG found in the Kinematic Analysis. In the right panel of Figure 10, we show the CMD for the  $\nu$ ,  $\omega$ ,  $\beta$  and  $\delta$  Sco substructures, as expected from their (X,Y,Z) and  $V_{T*}$  positions, we observe similar relative ages. We show 7, 8, 8 and 9 Myr isochrones for  $\nu$ ,  $\omega$ ,  $\delta$  and  $\delta$  Sco, respectively. We note that the global trend, better observed at the right of the age estimation interval, in the entire  $G-G_{RP}$  range is the expected from left panel of Figure 9.

#### 4.3.4 Age-velocity correlation

To further investigate the intrinsic  $V_{T*}$ -age trend, we define

$$\Delta V_{T*j} = \overline{V_{T*i}} - \overline{V_{T*\rho}} \quad (11)$$

where  $\overline{V_{T*j}}$  denotes the  $j$ -th substructure's mean value in the  $V_{T*}$  space and  $\overline{V_{T*\rho}}$  is the mean value of the  $\rho$  Oph substructure in the same space. We make note that 6 Myr is assumed as the maximum age of  $\rho$  Oph, but  $\overline{V_{T*\rho}}$  would be weighted by the full range of ages. Esplin & Luhman (2020) shown that the ages in  $\rho$  Oph range from 2 to 6 Myr. Hence, we adopt  $4 \pm 1$  Myr as the average age of  $\rho$  Oph and use this value for both plots in Figure 11. In the second and fourth columns of Table 4, we show  $\Delta V_{T*j}$  and the age estimations (with their respective upper and lower bounds) for each substructure. In upper panel of Figure 11 we show the  $\Delta V_{T*j}$ -age correlation with error bars denoting the upper and lower bounds reported in the age estimation.

If we assume a common linear drift rate, we are able to constrain the stellar populations in USco to be  $\sim 3.4 \pm 1$  Myr older for each  $\text{km s}^{-1}$  of separation with respect to  $\rho$  Oph in the  $V_{T*}$  space. However, note that there is an abrupt age difference between  $\delta$  Sco and  $\alpha$  Sco, despite their similar kinematic properties. There is a physical explanation to this in our picture: we expect that the parent molecular cloud of the substructures had similar kinematic properties than  $\alpha$  Sco, until the first SNe in  $\alpha$  Sco substructure induced a successive acceleration of their parent molecular cloud (as this is the main kinematic prediction of the triggered star formation scenario) towards the south west or en the direction of  $\rho$  Oph in the  $V_{T*}$  space. Therefore, we take this as a strong suggestion of triggered star formation as the origin of the substructures younger than  $\alpha$  Sco. We will discuss this with more detail in Section 5.4.

#### 4.3.5 Age-density correlation

We define the core volume of each substructure and the core mass enclosed by this volume as:

$$V_{\text{core}} = \frac{4\pi\epsilon_{\text{min}}^3}{3} \quad (12)$$

$$M_{\text{core}} = \text{MinPts} \times 0.4M_\odot = 12.4M_\odot \quad (13)$$

This definitions are based on the core definition in the context of the OPTICS algorithm (see Section 3.2.1 and do not take into account the irregularities in the spatial distribution.  $M_{\text{core}}$  is obtained by converting the mean absolute G magnitude in the USco KG to a mean mass of  $0.4 M_\odot$  based on the estimates from Pecaut & Mamajek (2013). Lower panel in Figure 11 shows the resultant empirical expansion law that correlates the density with the age of these substructures. This observational evidence suggests that each substructure expands with time at a logarithmic rate and may explain the presence of Diffuse populations as the expanded outer regions of

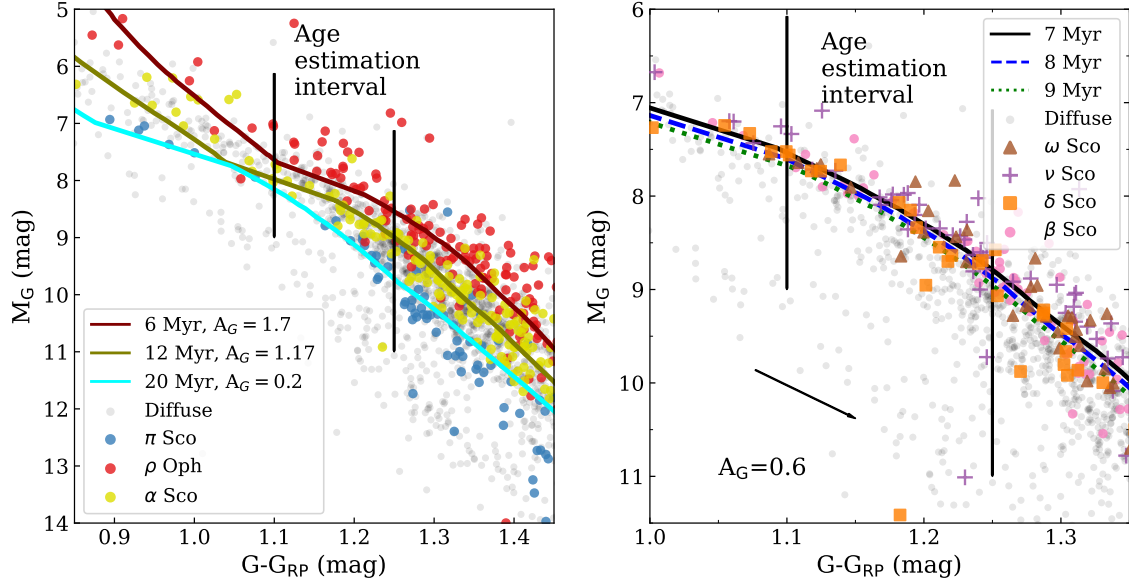


**Figure 10.** Left: CMD for the  $\rho$ ,  $\alpha$ ,  $\pi$  Sco substructures and the Diffuse populations with  $G-GRP$  colors and absolute G magnitude  $M_G$ . The maximum age of  $\rho$  Oph and the mean age of  $\alpha$  Sco and  $\pi$  Sco are fitted by PARSEC extinction-corrected 6, 14 and 20 Myr isochrones. Right: same as left but for the  $v$ ,  $\beta$ ,  $\omega$  and  $\delta$  Sco substructures. Mean ages of these substructures are fitted with PARSEC extinction-corrected ( $A_G=0.6$ ) 7, 8, 8 and 9 Myr isochrones. We include extinction vectors to illustrate the average effects of extinction. In both panels, vertical bars at  $G-GRP = 1.1$  and  $G-GRP = 1.25$  delimit our age estimation interval (see text for details).

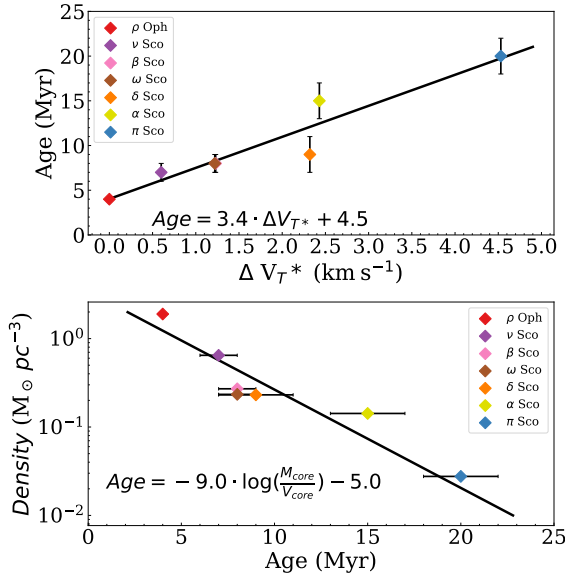


**Figure 11.** Top:  $\Delta V_{T^*}$  vs age. Bottom: age vs density. Upper and lower bounds for the photometric age estimates are shown.

the localized substructures found, rather than being in-situ formed populations or the result of the expansion of a unique global structure. The expansion rate probably depends on the specific formation conditions or mechanism for each structure, however, a global trend seems to be satisfied. Al though this important result escapes the

Substructure	$\Delta V_{T^*}$ [km s $^{-1}$ ]	$V_{core}$ [pc $^3$ ]	Age $_{phot}$ [Myr]
$\rho$ Oph	0	6.54	4 $\pm$ 1 6 (max)
$v$ Sco	0.60	19.16	7 $\pm$ 1
$\beta$ Sco	1.22	45.83	8 $\pm$ 1
$\omega$ Sco	1.22	52.99	8 $\pm$ 1
$\delta$ Sco	2.32	53.67	9 $\pm$ 2
$\alpha$ Sco	2.42	87.11	14 $\pm$ 2
$\pi$ Sco	4.52	448.92	20 $\pm$ 2

**Table 4.**  $V_{core}$  based on the  $\epsilon_{min}$  parameter,  $\Delta V_{T^*}$  calculated from Eq.(11) and Age estimated from the CMD in Figure 10, via PARSEC models and the average of the extinction estimates, with the statistic errors. As discussed in the text, the intrinsic ages are also affected by a systematic error of  $\sim 1$  Myr.

aims of this work, it deserves further investigation and further testing in other OB associations.

#### 4.4 General properties and massive content

We devote this section to summarize some important properties of the substructures discussed in section 4.3 that we consider relevant for the discussion in Section 6. We also estimate which stars from the Turn-Off sample belong to each substructure, justifying their names. We constrain the age of these stars based on Ekström et al. (2012) grids with rotation. In addition to the latter, this classification is also important to estimate the number of SNe events hosted by each substructure. To define if a star belongs to a given substructure, we consider mainly the spatial and celestial positions from Figure

Source Designation <sub>*</sub>	SpT <sup>A</sup>	Mass <sup>A</sup> [M <sub>⊙</sub> ]	Age <sup>A</sup> [Myr]	Age <sup>B</sup> [Myr]	Substructure	Age <sup>C</sup> [Myr]
$\tau$ Sco <sub>*</sub>	B0V	15±0.1	5.7±1	1	$\alpha$ Sco*	-
$\delta$ Sco <sub>*</sub>	B0.2IV	13 <sup>D</sup>	4.8±0.2	7	$\delta$ Sco	9±2
$\beta^1$ Sco <sub>*</sub>	B0.5V	12.5±0.6	13.8±0.4	7	$\beta$ Sco	8±1
$\sigma$ Sco <sub>*</sub>	B1III	18.7 <sup>E</sup>	8±0.2	8	$\alpha$ Sco	14±2
$\omega^1$ Sco <sub>*</sub>	B1V	11.1±0.9	10±5	1	$\omega$ Sco	8±1
$\pi$ Sco <sub>*</sub>	B1V+B2V**	12.5±0.6	15.3±0.6	10	$\pi$ Sco	20±2
1 Sco <sub>*</sub>	B1.5Vn	8.3±0.2	10.3±5.3	5	$\alpha$ Sco*	-
$\nu$ Sco <sub>*</sub>	B2IV	9.2±0.3	21±2.4	23	$\nu$ Sco	7±1
$\beta^2$ Sco <sub>*</sub>	B2V	7.3±0.1	2.3±2.2	<1	$\beta$ Sco	8±1
$\rho$ Sco <sub>*</sub>	B2IV-V	8.1±0.1	20.5±3.2	18	UCL	-
13 Sco <sub>*</sub>	B2V	7.8±0.1	2.9±1.8	15	UCL	-
$\alpha$ Sco <sub>*</sub>	M1.5Iab-b <sup>G</sup>	11-15 <sup>F</sup>	17.1±0.6	15 <sup>F</sup>	$\alpha$ Sco	14±2

**Table 5.** Rows: the Turn-Off sample plus  $\alpha$  Sco<sub>\*</sub>. Columns: 1. Designation for each star. 2. Spectral type and class. 3. Mass for the V stars is obtained from A. References are specified for the other luminosity classes. 4. Age from B. 5. Age from C. 6. Age assigned by correspondence with a substructure. 7. Parent structure. Given the mass and age from B and D, we are not able to associate  $\tau$  Sco<sub>\*</sub> to any substructure. References: A: (Tetzlaff et al. 2011), B: (Pecaut & Mamajek 2016), C: this work (by association with the substructures), D: (Miroshnichenko et al. 2013), E: (North et al. 2007), F: (Ohnaka et al. 2013), \*: potential corone member. \*\*:  $\pi$  Sco<sub>\*</sub> is a spectroscopic binary comprised of a pair of stars with the shown spectral types (Garrison 1967; Hiltner et al. 1969)

7 (lower panels), and Figure 8). However, there are several cases where is necessary to account for other physical considerations and some where is not possible to unambiguously relate a massive star to any substructure in particular. The results are summarized in Table , where the columns 7 and 8 constitute our age and upper mass-limit estimations.

#### 4.4.1 $\rho$ Oph: age cornerstone

Our substructure’s intrinsic age estimations are strongly based on the reported maximum age of 6 Myr for  $\rho$  Oph (Cánovas et al. 2019; Esplin & Luhman 2020). Hence, in section 4.3, we chose conservative  $\xi$  limits for the  $\rho$  Oph substructure, as we aimed to recover a confident sample, rather than an in depth survey of this well known region. We remark again that  $\rho$  Oph is composed by several smaller populations with ages between 0 (Pillitteri et al. 2016) and 6 (Esplin & Luhman 2020) Myr in a complex structure of stars and molecular clouds. We will revisit these properties in our proposed star formation scenario for USco in section 6.

#### 4.4.2 $\delta$ , $\beta$ , $\omega$ and $\nu$ Scorpii clusters

In previous sections we found that these substructures show a correlation in age-velocity, age-position and age-density, while they are also close in each of those spaces. We take the age-position correlation as the primary evidence of that an external triggering event induced the formation of these structures, while the other correlations independently support this scenario (see footnote 1).

$\nu$  Sco is named after the star Jabbah ( $\nu$  Scorpii<sub>\*</sub>), part of a hierarchical system with 7 components (Tokovinin 2018).  $\nu$  Sco and  $\rho$  Oph barycenters are 13 pc away in the Z direction, while their dispersion in that direction is about  $\sim 4.5$  pc, however, their kinematic properties and positions in the CMD are very similar, suggesting a common mechanism for their formation and constraining the expected position of a potential triggering event towards the east. Moreover, they are both close to prominent molecular clouds located westwards (see Lynds clouds in Figure 8).  $\beta$  Sco is named after the star Acrab ( $\beta^1$  Sco<sub>\*</sub>). We recognize that there is a large difference between the distance to the cluster and the star. However,

orbital motions due to its binary nature certainly affect the parallax measurements, which are from Hipparcos. This can be seen from the  $V_T$  positions of the pair, which locates them outside the USco KG. Hence, we argue that the distance of the pair is very likely to be underestimated due to its orbital motions and we expect it belong to the  $\beta$  Sco substructure.  $\omega$  Sco is named after  $\omega^1$  Sco<sub>\*</sub> which is expected to be a single star (Pecaut et al. 2012) and has spatial a celestial position within the boundaries of the respective structure. We note a high RUWE value ( $\sim 2.4$ ) for this star, suggesting that is probable that has a unresolved secondary. If verified, all the most massive stars in this substructures would be actually binaries or hierarchical systems.  $\delta$  Sco is named after Dschubba ( $\delta$  Sco<sub>\*</sub>). We base the relation between these systems mainly on their celestial position and kinematics.

#### 4.4.3 $\pi$ Scorpii: the missing link

$\pi$  Sco is named after the system Fang ( $\pi$  Sco<sub>\*</sub>), a spectroscopic binary comprised of a pair of stars with the spectral types B1V and B2V (Garrison 1967; Hiltner et al. 1969), or  $\sim 12$  and  $\sim 7$  solar masses. There is some ambiguity regarding the actual position in space of this system given that: the Gaia eDR3 distance to this binary star is  $\sim 70$  pc lower than the Hipparcos distance, but the Gaia eDR3 parallax error is larger than its Hipparcos counterpart, however, the resultant parallax over error value is bigger in the Gaia eDR3 catalog,  $\sim 14\%$ , with respect to the Hipparcos value of  $\sim 8.7\%$ . On the other hand, all the members that give their name to the substructures have extinction values  $A_V$  remarkably similar to the mean  $A_V$  of the substructures, which makes sense if they are embedded into the same clouds as their parent substructure.  $\pi$  Sco<sub>\*</sub> is no exception to this with  $A_V = 0.2$  mag, while  $A_V$  for  $\pi$  Sco = 0.23 mag. At  $\pi$  Sco<sub>\*</sub> sky position, if it were far behind the respective substructure we would expect it to have an extinction notably larger than 0.23 mag, as it is the case for 1 Sco with  $A_V = 0.46$  mag. After considering this, we assign this system as a member of the respective substructure. However, this is an important caveat which needs further study. A precise estimation of fundamental parameters of Fang escapes our aims, but the mass of the B1V component is still well above the lower mass limit of the Turn-Off sample, hence,



we include it as a massive member of  $\pi$  Sco and a potential SNe progenitor.

Remarkably,  $\pi$  Sco overlaps with the region of high probability to be the origin of a SNe event  $\sim -1.5$  Myr ago in the outskirts of both USco, as reported by Breitschwerdt et al. (2016). This region is centered at  $(X,Y,Z) = (83,-25,41)$  pc while  $\pi$  Sco is located at  $(X,Y,Z) = (101,-19, 39)$  pc (see Figure 7). However, the study of Neuhäuser et al. (2020) on the runaway star  $\zeta$  Oph (Hoogerwerf et al. 2000), provides a correction on the time and present-day location of the event,  $1.78 \pm 0.21$  Myr ago and  $(X,Y,Z) = (99,-34,25)$  pc (see Neuhäuser et al. (2020), its Table 4), respectively, locating it even closer at no more than 5 pc from  $\pi$  Sco and. We take this as strong evidence of  $\pi$  Sco being the parent structure of both  $\zeta$  Ophiuchi and the progenitor of the SNe event that expelled it. This intrinsic relation provides valuable information for both the objects and the structure. For example, there is a large uncertainty on the mass of  $\zeta$  Oph,  $13_{-6}^{+10}$ , and the mass of its progenitor strongly depends on the age of the structure that hosted it. Indeed, Neuhäuser et al. (2020) estimated the mass of this progenitor as  $17 \pm 2 M_{\odot}$  based on an age of 12-15 Myr from the age map in Pecaut & Mamajek (2016). We stress here that this age map is a sky projection, so that it does not excludes the possibility of having an older substructure in foreground, as we suggest for  $\pi$  Sco. Hence, our age for  $\pi$  Sco implies a new mass for the progenitor of  $11.8 M_{\odot}$  (see Table 6).

Remarkably, a Bubble in the ISM was found by Robitaille et al. (2018) in the Planck data (Planck Collaboration et al. 2011). Robitaille et al. (2018) suggested that this Bubble may be a  $\sim 3$  Myr old SN remnant at a distance of  $\sim 139 \pm 10$  pm, with its shell interacting with both  $\rho$  Oph and Lupus clouds. While the spatial description is consistent with the observed voids in Figure 7, a recent SN event in  $\pi$  Sco makes it more plausible for the Bubble to be related with the Void 2.

#### 4.4.4 $\alpha$ Scorpii moving group

This substructure is the largest, roughly coeval and compact structure in USco. It belongs to the  $\alpha$  KG retrieved from the Kinematic Analysis. Its notable size, its relation with the  $\alpha$  KG and the conclusions from section 4.3.2 suggest that is largely disperse and, hence, that is the origin of many other loose members from the Diffuse populations. Given its age, we expect that stars with  $M > 1.6 M_{\odot}$  (SpT  $\sim$  F0) have already entered the H-burning phase (Siess et al. 2000), suggesting a negligible number of A stars from this population in the OB sample.

$\alpha$  Sco is named after the star Antares ( $\alpha$  Sco<sub>\*</sub>). Antares has an age and mass of 11-15 Myr and  $15 \pm 5 M_{\odot}$  (Pecaut et al. 2012; Ohnaka et al. 2013), which is consistent with the estimated age of 14 Myr and the upper mass-limit of  $14.9_{-1.4}^{+1.8} M_{\odot}$  for this substructure. Similarly, the star Alniyat ( $\sigma$  Sco<sub>\*</sub>) has a mass of  $18.4 \pm 5.4$ , which is also consistent with the upper mass-limit for the substructure. Furthermore, we able to relate the system EPIC 203710387, an eclipsing binary system with constrained age from David et al. (2019), to the  $\alpha$  Sco substructure. According to the authors, EPIC 203710387 should have  $\sim 12 \pm 3$  Myr in PARSEC V1.1, which is consistent with our assigned age of  $\sim 14 \pm 2$  Myr with the same isochrone model.

We assign both stars to this substructure by further considering their spatial positions. Note from Figure 7 that is the nearest structure to these stars, so that if they do not belong to it, they must be runaways from the younger structures. We rule out the former scenario for Antares, based on its estimated age and mass. For Alniyat, the age estimates of  $\sim 8$  Myr seem to be consistent with this case, however, we also consider that the typical mass of  $\beta$  Ceph stars is  $\sim$

$12 M_{\odot}$  and the fact that its distance seems to be systematically underestimated. Furthermore, from a canonical IMF, we expect more that one massive member for this substructure, as it doubles the stellar content of the others, despite of a large fraction of its members being already too disperse to be classified as such. Based on the latter, we argue that is more likely that the mass and age of Alniyat to have been over and sub-estimated, respectively, than it being a runaway star or have formed in situ. We classify the stars  $\tau$  Sco<sub>\*</sub> and  $1$  Sco<sub>\*</sub> as potential coroneae members of  $\alpha$  Sco. However,  $\tau$  Sco<sub>\*</sub> seems to be too massive and too young to have formed in this substructure and  $1$  Sco<sub>\*</sub> classification as such results ambiguous due to its large distance from  $\alpha$  Sco.

#### 4.5 SNe in USco

To obtain  $N_{\text{SN}}$ , we follow the procedure sketched in Sect 3.3. We obtained that only the substructures  $\pi$  Sco and  $\alpha$  Sco have possibly hosted at least 1 SNe in the past, so we focus our exposition on these substructures. The input parameters for each substructure are  $N$ ,  $M\tau$  and  $M_{\text{up}}$ , where  $N$  is the number of stars with  $M > 7.3 M_{\odot}$  (SpT  $< \sim$  B2V),  $M\tau$  is the mass of a SNe progenitor occurred at the time  $\tau$  after the structure's birth and  $M_{\text{up}}$  is the mass of the most massive member in the given structure. The introduction of parameters is not straightforward, for example, in section 4.4 we obtained with certainty that  $N=2$  for  $\pi$  Sco but  $N$  may be 2, 3 or 4 for  $\alpha$  Sco, so we evaluate three cases for this substructure. On the other hand, we lack precision on the mass of the most massive member for both substructures and the occurring times and progenitor mass for the SNe are very sensible to this value. We were able to solve the  $M_{\text{up}}$  problem in a consistent manner for each substructure. The most massive star in  $\alpha$  Sco is Antares, which is already in the He-burning phase, hence, its mass is somewhere between the upper mass for H-burning and the upper mass for He-burning, where both depend on the age  $\alpha$  Sco. This way, we obtain the mass of Antares and the SNe occurring times with uncertainty  $< 1 M_{\odot}$  and 1 Myr in the full range of the uncertainty for the age of  $\alpha$  Sco. For  $\pi$  Sco, we use the occurring time of the SNe that expelled  $\zeta$  Oph:  $1.78 \pm 0.21$  Myr (see Section 4.4.4); for a given age of  $\pi$  Sco, we only have to find the progenitor mass of a SNe that occurred at that time. This mass depends on the age of  $\pi$  Sco, so we also explored the upper and lower bounds of its age. For the remaining substructures, we obtain the normalization constant based on the upper limit-mass and estimate  $N_{\text{SN}}$  based on the masses from Table 5. For the remaining substructures, we obtain  $N_{\text{SN}} < 1$ . Remarkably, this implies that the present day mass function is identical to the IMF in these substructures. However, we note that the upper mass values notably differ from the measured values, most dramatically in the case of the  $\nu$  substructure, in contrast with the observed on the previously discussed substructures where the difference was minimal. The latter may be consequence of the structures being smaller or evidence of a more fundamental relation between the IMF and the respective formation mechanism. This is an important result that deserves further investigation and we will revisit this in future work.

Via this procedure, we obtain that at least 3 and up to 4 SNe have occurred in USco. 2 hosted by  $\pi$  Sco  $\sim 10$  and 1.78 Myr ago and 1 or 2 hosted by  $\alpha$  Sco with occurring times depending on  $N$  in Table 6. Note that the 3 values of  $N$  and age for  $\alpha$  Sco yield a SNe  $\sim 10 \pm 2$  Myr ago, allowing us to conclude that a SNe certainly happened around this time. However, the mass of the progenitor of this SNe largely depends on the assumed age for  $\alpha$  Sco. For  $N = 3, 4$ , we obtain a second event  $\sim 5$ -6 Myr ago. Hence, we obtain that 2 SNe occurred  $\sim 10 \pm 2$  Myr ago, another  $\sim 5$  Myr ago and a more recent

Structure	N	Age [Myr]	H-M <sub>up</sub> [M <sub>⊙</sub> ]	He-M <sub>up</sub> [M <sub>⊙</sub> ]	M <sub>up</sub> [M <sub>⊙</sub> ]	N <sub>SN</sub>	k	τ <sub>1</sub> [Myr]	M <sub>1</sub> [M <sub>⊙</sub> ]	τ <sub>2</sub> [Myr]	M <sub>2</sub> [M <sub>⊙</sub> ]
π Scorpii	2	20 <sup>+2</sup> <sub>-2</sub>	11.5 <sup>-0.6</sup> <sub>+0.7</sub>	12.2 <sup>-0.6</sup> <sub>+0.8</sub>	12.9 <sup>-0.8</sup> <sub>+1.1</sub>	1.7 <sup>+0.3</sup> <sub>-0.3</sub>	73.9 <sup>+6.2</sup> <sub>-6.3</sub>	-11.1 <sup>-0.4</sup> <sub>+0.1</sub>	32.0 <sup>-8</sup> <sub>+20</sub>	-	-
	2					1.2 <sup>+0.3</sup> <sub>-0.3</sub>	63 <sup>+6.2</sup> <sub>-5.2</sub>	-8.7 <sup>+0.4</sup> <sub>-0.8</sub>	38.4 <sup>-14</sup> <sub>+85</sub>		
α Scorpii	3	14 <sup>+2</sup> <sub>-2</sub>	14.5 <sup>-1.4</sup> <sub>+2</sub>	15.8 <sup>-1.6</sup> <sub>+2</sub>	14.9 <sup>-1.4</sup> <sub>+1.8</sub>	1.7 <sup>+0.5</sup> <sub>-0.4</sub>	95.8 <sup>+9.5</sup> <sub>-8</sub>	-12 <sup>+1</sup> <sub>-0.2</sub>	181 <sup>+60</sup> <sub>-140</sub>	-5.8 <sup>-0.1</sup> <sub>+0.01</sub>	22.5 <sup>-3.6</sup> <sub>+9</sub>
	4					2.3 <sup>+0.6</sup> <sub>-0.5</sub>	127 <sup>+12.5</sup> <sub>-10.5</sub>	-8.7 <sup>+0.4</sup> <sub>-0.8</sub>	38.4 <sup>-14</sup> <sub>+85</sub>	-4.5 <sup>+0.3</sup> <sub>+0.3</sub>	19.7 <sup>-2.8</sup> <sub>+4.1</sub>
δ Scorpii	1	9 <sup>+2</sup> <sub>-2</sub>	21.1 <sup>-3.4</sup> <sub>+8.6</sub>	23.2 <sup>-4.1</sup> <sub>+9.9</sub>	13	<0.63	22 <sup>+2</sup> <sub>-2</sub>	-	-	-	-
β Scorpii	1	8 <sup>+1</sup> <sub>-1</sub>	24.5 <sup>-3.4</sup> <sub>+5.2</sub>	27.4 <sup>-4.2</sup> <sub>+5.7</sub>	12.5	<0.62	21 <sup>+1.3</sup> <sub>-1.2</sub>	-	-	-	-
ω Scorpii	1	8 <sup>+1</sup> <sub>-1</sub>	24.5 <sup>-3.4</sup> <sub>+5.2</sub>	27.4 <sup>-4.2</sup> <sub>+5.7</sub>	11.1	<0.73	21 <sup>+1.3</sup> <sub>-1.2</sub>	-	-	-	-
ν Scorpii	1	7 <sup>+1</sup> <sub>-1</sub>	29.7 <sup>-5.2</sup> <sub>+7.3</sub>	33.0 <sup>-5.6</sup> <sub>+8.2</sub>	9.2	<0.89	20 <sup>+1.2</sup> <sub>-0.9</sub>	-	-	-	-

**Table 6.** Rows: stellar evolution parameters for each substructure. Columns: 1. Substructure’s name. 2. The number of stars with mass  $> 7.3 M_{\odot}$ . 3. Substructures age with statistical uncertainty. 4. Expected upper limit for the mass of H-burning stars. 5. Expected upper limit for the mass of He-burning stars. 6. Mass of the more massive star. For α and π Sco, is the mass of Antares and ζ Ophiuchi’s companion. 7. N<sub>SN</sub> results (see Section 3.3). 8. Normalization constant (see Section 3.3) 9. Occurrence time for the first SNe retrieved. 10. Mass of progenitor at τ<sub>1</sub>. 11. 12. Mass of progenitor at τ<sub>2</sub>.

one, the one that would have expelled ζ Oph, 1.78 Myr ago. We base mainly on this, the internal structure of USco and the age gradients observed to suggest a star formation scenario for USco in section 5.4.

## 5 DISCUSSION

### 5.1 Robust substructure retrieval

It is straightforward to conclude from Sect 4.2 that the spatial distribution of the KGs is genuinely complex, justifying the need of the Spatial Analysis (see Section 3.2) to extract more information from this region. Moreover, evidence of substructure in USco with Gaia DR2 (Kerr et al. 2021) and Gaia eDR3 (Squicciarini et al. 2021) has already been found. However, there are important differences between our results and those of these works due to the different procedures and the improved precision of Gaia eDR3. For example, Kerr et al. (2021) recovers 7 substructures in USco. However, the authors set the prior of spatial substructures in USco to be clustered in the transverse velocity space, which is physically expected, but, given how close the substructures retrieved are in this kinematic space and that the typical errors in Gaia DR2 (Gaia Collaboration et al. 2018) increase by a factor of 3 to 4 in proper motion and 30–50% in parallax, we argue that this is not a good empiric assumption in the particular case of USco (see Section 1) and Section 3.2.1). We have also shown how unresolved binaries would introduce a strong bias into this assumption in Sect 4.3.2. Squicciarini et al. (2021) recovers 8 substructures in USco by tracing back in time the position of the sources in USco and applying a k-means clustering. The authors validate the physical relevance of some of the substructures retrieved via a visual comparison with the results from Kerr et al. (2021), while recognize that 2–3 of them require further investigation.

We were able to unambiguously relate substructures 17-E, 17-G, 17-I and 13 from Kerr et al. (2021) to ν Sco, β Sco, ρ Oph and π Sco, respectively. Our Spatial Analysis suggests that their substructure 17-H is actually composed by ω and δ Sco, while substructures 17-B and 17-C are contained within the larger α Sco. Finally, 17-A and 17-F do not have any counterpart in our work, probably due to the reasons discussed previously in this section. On the other hand, substructures 1, 2 and 6 from Squicciarini et al. (2021) have share

sky positions and tangential velocities with ρ Oph, ν Sco and β Sco. Substructures 3 and 4 have similar sky positions to ω Sco and δ Sco, but notably different kinematics. Correspondence between substructures 3, 7 and 8 with any of our work is ambiguous and hard to conclude since we do not have access to this data. From this comparison, we show that we are able to significantly extend the membership and improve the characterization of the already known structures ν Sco, β Sco, and π Sco, while our analysis clearly distinguishes the presence, spatial and kinematic clustering of the structures α Sco, ω Sco and δ Sco via the sum of independent methods in a multidimensional approach. We are also able to relate for the first time these substructures with the massive stars after which they are named, and provide quantitative evidence (the ε and ξ parameters) of their clustered nature.

### 5.2 The age of USco

USco has been historically treated as a coeval population younger than the other groups in Sco-Cen. However, in section 4.3.1 we show that USco is far from coeval in the Myr scale, as there are stellar objects with ages ranging from 0 to ~ 20 Myr. Moreover, we not only observe a large age dispersion, but also show that several distinct populations are responsible for this spread. We recover a mean age of ~ 9.4 Myr based on the substructures shown in Figure 10. Our results are in agreement with previous recent estimations of ~ 10 Myr as the global age of USco with a broad variety of methods (e.g., Pecaut et al. 2012; Pecaut & Mamajek 2016; Sullivan & Kraus 2021; Kerr et al. 2021), with the exception of the estimated age of 4.5±0.1 Myr for the clustered populations and 8.2±0.1 Myr for the diffuse populations by Squicciarini et al. (2021). However, we note that relative ages between common structures are in agreement. We restate the previous conclusions of USco being younger than the other groups in Sco-Cen as it having a large fraction of younger populations than the other groups, biasing its average age towards the 10 Myr value, but its older structures, α and π Scorpii, are roughly coeval with the other groups in Sco-Cen. Moreover, the presence of these substructures and the massive stars associated with each also explains why these massive members do not span a clear turn-off sequence (Pecaut et al. 2012; Pecaut & Mamajek 2016). This work also constrains the age of several of the most massive members in USco, which yield differences > 10 Myr between

their ages. Of course, this age difference extends to the mid and low mass populations, hence, future works would have to consider the positions, kinematics, dynamics and ages of these substructures, observationally constrained in this work, for the full mass range in the USco region. This improvement in the resolution of these properties makes USco an even more valuable region as it spans multiple young populations with now resolvable ages that will make it possible to further constrain processes of planetary formation, early stellar evolution and star formation.

### 5.3 USco: home of near Earth supernovae

In section 4.5 we have shown that it is very likely that 3 to 4 SNe events have occurred in  $\alpha$  Sco:  $\sim 10 \pm 2$  (SN<sub>A1</sub>) and  $5 \pm 1$  (SN<sub>B</sub>) Myr ago, and in  $\pi$  Sco:  $\sim 10 \pm 2$  (SN<sub>A2</sub>) and  $2$  (SN<sub>C</sub>) Myr ago. Here we briefly discuss these events in relation with some previous work. There is a copious amount of evidence for  $^{60}\text{Fe}$  ejecta from recent  $< 10$  Myr SNe events to have reached the Earth (see Miller et al. (2022), its Figure 1 and references therein). In this regard, the candidates to have hosted these events are Sco-Cen and the Tucanae-Horologium (Tuc-Hor) associations (Benítez et al. 2002; Fuchs et al. 2006; Mamajek 2016). Although some models favor Tuc-Hor when trying to explain the recent  $\sim 2.2$  Myr  $^{60}\text{Fe}$  peak (e.g., Fry et al. 2016; Miller & Fields 2022), only one SNe event is speculated to have occurred in this association, making it necessary to look somewhere else when trying to explain the more ancient  $\sim 7$  Myr peak in the  $^{60}\text{Fe}$  income.

Chaikin et al. (2022) concludes a realistic signal can be produced by a SN in the distance range of 10 to 200 pc and requires two SNe to explain the observed  $^{60}\text{Fe}$  peaks. Based on this we suggest a contribution from the expected SN<sub>A1</sub> and SN<sub>A2</sub> events to the 7 Myr peak. This is also consistent with the results of Sørensen et al. (2017), that reports a peak in the SNe events in the solar neighborhood 10 Myr ago. The recent 2.2 Myr peak may be explained by the SN<sub>B</sub> event. For the ejecta from the recent SN<sub>C</sub> we can conceive 2 possibilities: 1. It is about to reach the Earth as it was similarly concluded by Neuhäuser et al. (2020), or 2. If we relax the uncertainty in the occurrence time of the SN<sub>C</sub>, justified by the age estimation of the Robitaille et al. (2018) Bubble (3 Myr), the SN<sub>C</sub> may have also contributed to the 2.2 Myr peak. Some considerations which prevents us to go beyond suggesting this scenarios are the following: 1. Given that SN<sub>B</sub> position is highly uncertain, the  $\alpha$  Sco distance of  $\sim 160$  pc may be too far for its SN<sub>A2</sub> ejecta to reach us (e.g., Fry et al. 2016; Miller & Fields 2022). 2. The  $^{60}\text{Fe}$  peaks may be the result of a complex chain of SNe events, instead of just one per peak, as it was found by Wallner et al. (2016a). 3. The expected distances and reaching times rely on assumptions like a uniform ISM and a given velocity of the solar system with respect to the SNe shock front Chaikin et al. (2022).

On the other hand, Forbes et al. (2021) investigated the origin of the observed amount of  $^{26}\text{Al}$  radionuclide in the Ophiuchus clouds and leaves the age of USco as a free parameter to constrain its source from being stellar winds and SNe in different proportions. To this date only  $1 \pm 1$  SNe was expected to have occurred in USco (de Geus 1992) given it was assumed to be 5 Myr when this estimation was last performed. In this work show that at least 3 and up to 4 SNe have occurred in USco at different times in the last  $\sim 12$  Myr. In this sense, our results partially constrain the source type of  $^{26}\text{Al}$ , since we update the age of USco and its internal stellar populations and, consequentially, the amount of expected SNe in the region. In this regard, a recalculation of energy input of the USco-Shell considering contribution of the stellar winds of the missing massive stars and the respective SNe events becomes necessary. This, together with the

$^{26}\text{Al}$  constrains, would place tighter constraints on how many SNe have actually gone off in USco. However, this matter escapes the aims of our work.

We report the discovery of  $\pi$  Sco being the structure that hosted the SNe event that expelled  $\zeta$  Oph (Neuhäuser et al. 2020), which has been also suggested to be one of the two nearest SNe events to Earth (Breitschwerdt et al. 2016).

### 5.4 Star formation history

A plausible scenario for the star formation history (SFH) of Sco-Cen was proposed by Kerr et al. (2021). However, the SFH of USco has been subject of debate for decades (e.g., de Geus 1992; Preibisch & Zinnecker 1999; Preibisch & Mamajek 2008; Pecalet et al. 2012; Pecalet & Mamajek 2016; Damiani et al. 2019; Luhman & Esplin 2020; Squicciarini et al. 2021). Here we suggest a SFH with unprecedented time-resolution based on the uncovered spatial, kinematic and age substructure of USco that allowed us to recover potential past SNe events in this region and find evidence of the kinematic imprints of the progenitors on the young stellar populations. Our proposed scenario is focused on explaining how the substructures  $\rho$  Oph,  $\nu$  Sco,  $\beta$  Sco,  $\omega$  Sco, and  $\delta$  Sco were formed. We suggest that the substructures retrieved are the result of a complex chaining of triggering events associated with the expected SNe events and the stellar winds of their massive progenitors. In our scenario, expanding shells powered by the progenitor winds and remnants of the SN<sub>A1</sub> and SN<sub>A2</sub> triggered the compression of the molecular clouds between them at their encounter fronts  $\sim 10$  Myr ago, whose collapse had been already stopped or slowed down by the stellar winds of their massive progenitors. These events would have induced the formation of the  $\delta$  Sco,  $\beta$  Sco,  $\omega$  Sco,  $\nu$  Sco substructures, leaving as evidence the age gradients observed today in Figures 9, 10 and 11. SN<sub>B</sub> and SN<sub>C</sub> events would have further triggered star formation in the  $\rho$  Oph molecular cloud complex. We base these conclusions on the following:

- The age-position gradient and small size of the substructures with age  $< 10$  Myr (see Figure 7 and Table 3) plus their age-velocity and age-density correlations (see Section 4.3.4) suggest an external triggering event, as their parent molecular cloud probably did not have enough mass to collapse at the time the more massive  $\alpha$  Sco was formed.
- In Figure 7, we observe two regions (Void 1 and Void 2) with an apparent lack of stars or dense regions. These voids are well fit by ellipsoids with semi axes in the outskirts of  $\pi$  Sco and  $\alpha$  Sco. The remaining substructures lay between these voids and separate them. This ellipsoidal geometry is not likely to be coincidental and it also correlates with the age-position gradient. Hence, we deduce that the lack of stars in these regions is the result of a true physical process, i.e., stellar winds from the progenitors of SN<sub>A1</sub> and SN<sub>A2</sub> altering the dynamics and geometry of the ancient molecular clouds.
- One these above mentioned progenitors was hosted by  $\alpha$  Sco and the other by  $\pi$  Sco on the opposite sides of the younger substructures, which are located at the edges of these voids.
- The occurring time of SN<sub>A1</sub> and SN<sub>A2</sub> coincides with the maximum age of  $\delta$  Sco.
- The global age of  $\rho$  Oph complex can be explained by the above mentioned scenario, but its internal ages do not show any clear directionality. Recently, Gupta & Chen (2022) found that more evolved stars are farther from the denser clouds and suggest that the shape of the cloud B in its Figure 1 is due to the shocks of the stars belonging

to our  $\alpha$  Sco substructure. This morphology, we argue, may also be explained by the effect of  $\text{SN}_B$  and  $\text{SN}_C$  events.

- The occurring time of the  $\text{SN}_B$  is remarkably consistent with the maximum age of  $\rho$  Oph complex, suggesting that it could have re-activated or definitely induced star formation in the complex.
- Our scenario is consistent with the predicted star formation mechanism in Sco-Cen by Krause et al. (2018), based on different observations before Gaia-DR2. Krause et al. (2018) concluded that similar a scenario is the predominant mechanism for star formation in Sco-Cen and possibly other OB associations and questioned the independence of the star formation in Lupus I and  $\rho$  Oph clouds. Hence, the  $\text{SN}_C$  may be responsible for the most recent star formation activity in the  $\rho$  Oph and Lupus clouds, in agreement also with the scenario suggested by Gaczkowski et al. (2017a).
- A similar formation scenario has been proposed in specific for the Lupus I clouds by Gaczkowski et al. (2017b), where the recent star formation in this region would be the result of the interaction between the USco Shell and the stellar winds from B stars in UCL. In this respect, we also observe that the Void 2 limits with the Lupus I clouds, extending our scenario to that region and supporting their conclusions. Moreover, as we have mentioned, we expect that the progenitor of the expected SNe events would also have contributed to the Voids and the arrangement of the  $< 10$  Myr substructures' parent clouds.
- The age and location of the clouds in USco, USco-Shell (5.7 Myr) and USco-Loop (1 Myr) (Pöppel et al. 2010), coincide remarkably well with both the occurring times and locations of the  $\text{SN}_B$  and  $\text{SN}_C$  respectively, implying that these structures are the remnants of these SNe events.
- The  $\sim 3$  Myr old bubble observed by Robitaille et al. (2018) overlapping with the  $\pi$  Sco age and position, which the authors suggest can be originated by a SN remnant with its shells interacting with both  $\rho$  Oph and Lupus clouds.

Additionally each SN-triggering event is supported by or explains several independent observations.  $\text{SN}_{A1}$  and  $\text{SN}_{A2}$ : the voids and geometry observed in Figure 7, the existence of the age, density and kinematic gradients of the structures located between  $\pi$  Sco and  $\alpha$  Sco.  $\text{SN}_B$ : the maximum of the  $\rho$  Oph complex, the Lupus I suggested formation scenario and the USco-Shell.  $\text{SN}_C$ : the  $\zeta$  Ophiuchi runaway star. All of these observations point to and are unified by the proposed scenario.

## 6 SUMMARY AND CONCLUSIONS

In the following, we summarize the main results of this work:

1. We retrieve a sample of 3661 candidate members for Upper Scorpius (USco) from the Gaia-eDR3 catalog, with an estimated contamination of  $\sim 9\%$  from Galactic field, and successfully validate it with the previous work from (Damiani et al. 2019; Luhman 2022). We also compile an astrometrically cleaner sample of 3004 sources with  $\sim 6\%$  of contamination (see Table 2).
2. We show that Upper Scorpius is composed by three main Kinematic Groups (KGs) with a clear age trend (see Figure 5) and a complex spatial distribution (see Figure 6). Remarkably, we note that single KGs are related to multiple spatial overdensities, suggesting that kinematic-only clustering spaces do are not enough to resolve all the spatial substructure in USco (and probably in other young associations).
3. To further investigate the spatial distribution of the KGs, we make use of the OPTICS algorithm (Ankerst et al. 1999). We apply OPTICS in the Heliocentric coordinates (X,Y,Z) space to ex-

clude any bias due to non-negligible errors and kinematically undistinguishable stellar populations. This analysis produces robust evidence of the presence of seven clustered substructures with the suggested names:  $\pi$  Scorpii (20 Myr),  $\alpha$  Scorpii (14 Myr),  $\delta$  Scorpii (9 Myr),  $\beta$  Scorpii (8 Myr),  $\omega$  Scorpii (8 Myr) and  $\nu$  Scorpii (7 Myr), after their most massive member, plus the well known  $\rho$  Ophiuchi substructure and a component of loose populations spanning the entire region (see Figure 7).

4. We constrain the membership, age and upper mass limit of several massive members in USco, including Antares (see Table 5 and Table 6). We also have found that  $\omega^1$  Sco is very likely to have an unresolved binary companion.

5. We observe two quasi-ellipsoidal stellar Voids which probably trace the stellar feedback from ancient massive stars (see Figure 7). The denser and younger regions in USco are located at the edges of these Voids. This fact, suggests that the now-gone massive members shaped and induced the subsequent star formation in the region.

6. We constrain the occurrence of two SN events, hosted by the  $\alpha$  Sco and  $\pi$  Sco substructures,  $\sim 10 \pm 2$  Myr ago, a third SN hosted by  $\alpha$  Sco  $\sim 5 \pm 1$  Myr ago and a fourth  $\sim 2$  Myr ago hosted by  $\pi$  Sco. We identify the latter with the event that expelled the  $\zeta$  Ophiuchi runaway star.

7. We observe an age-position and age-velocity correlation in the spatial substructures found in USco (see left panel in Figure 9). We base on this correlations to propose an star formation inducing event coming from the east. We identify this event with the expanding shells centered in the Voids and powered by the stellar feedback of the missing massive stars that went off as SN  $\sim 10 \pm 2$  Myr ago.

8. We suggest a star formation history for USco in which 4 ancient massive stars from  $\alpha$  Sco and  $\pi$  Sco shaped its present structure via their stellar winds and SNe explosions. In this scenario, the younger substructures  $\delta$  Sco,  $\beta$  Sco,  $\omega$  Sco,  $\nu$  Sco and  $\rho$  Oph are located between two stellar voids caused by the mentioned feedback events and they trace its influence with trends in their positions, kinematics, age and density.

9. This scenario is similar to that proposed by Krause et al. (2018) and we support the hypothesis of a common origin for the  $\rho$  Oph complex and the Lupus I clouds (Gaczkowski et al. 2017a). Additionally, the latter would be the SN event that expelled the runaway star  $\zeta$  Oph (Hoogerwerf et al. 2000; Neuhäuser et al. 2020). All these events would also be related to the observed peaks in  $^{60}\text{Fe}$  depositions measured on Earth (Wallner et al. 2016b). The occurring times, masses and other parameters of interest associated to this events are summarized in Table 6.

10. We suggest a direct relation between the proposed SNe events in USco and other independent observations, like the  $^{60}\text{Fe}$  peaks observed in the Earth and the Moon in the last  $\sim 10$  Myr (Wallner et al. 2016b), the  $^{26}\text{Al}$  abundance observed in USco (Forbes et al. 2021), the structure of the  $\rho$  Ophiuchi molecular clouds (Gupta & Chen 2022), recent star formation in the  $\rho$  Ophiuchi and Lupus clouds (Gaczkowski et al. 2017b), the well known USco Shell (de Geus 1992) and a recently found Bubble in USco (Robitaille et al. 2018).

11. We provide an empirical expansion law for the substructures in USco (see lower panel in Figure 11). We base on this law we suggest that the loose populations of USco, and probably the other groups in Sco-Cen, have origin in the core regions rather than being formed in situ. We make note that the assumption that the expansion rate is global does not takes into account key factors like the formation mechanism for each substructure and the different initial conditions. The universality of this law is to be tested in future work.



## ACKNOWLEDGEMENTS

Authors acknowledge the referee Eric Mamajek for the very insightful comments that helped to improve this work. Authors also acknowledge Kevin Luhman for comments and discussion on the membership validation of our census, Ralph Neuhauser for comments and discussion about our scenario in which  $\pi$  Sco hosted the recent supernova event that expelled the star  $\zeta$  Ophiuchi and the update of the mass of this supernova progenitor, and Manuela Zoccali for general comments about the Kinematic Groups found in Section 4.2. GBM also acknowledges David Sánchez Elizondo for discussions on nature, phenomena and causality, and support from Central American and Caribbean Bridge in Astrophysics (Cenca Bridge), Astrofísica Centroamericana y del Caribe (Alpha-Cen) and Centro Latinoamericano de Física, subsele Centroamérica (CLAF-CA). JC acknowledges support from the Agencia Nacional de Investigación y Desarrollo (ANID), via Proyecto FONDECYT Regular 1191366, and by the ANID BASAL projects CATA-Puente ACE210002 and CATA2-FB210003.

## DATA AVAILABILITY

This work presents results from the European Space Agency (ESA) space mission Gaia. Gaia data are being processed by the Gaia Data Processing and Analysis Consortium (DPAC). Funding for the DPAC is provided by national institutions, in particular the institutions participating in the Gaia MultiLateral Agreement (MLA). The Gaia mission website is <https://www.cosmos.esa.int/gaia>. The Gaia archive website is <https://archives.esac.esa.int/gaia>. The data from Table 2 will be available via the VizieR-Strasbourg service.

## REFERENCES

- Ankerst M., Breunig M., Kriegl H.-P., Sander J., 1999, in *ACM SIGMOD Record*, pp 49–60, doi:10.1145/304182.304187
- Barrientos M., Chanamé J., 2021, *ApJ*, **923**, 181
- Benítez N., Maíz-Apellániz J., Canelles M., 2002, *Phys. Rev. Lett.*, **88**, 081101
- Blaauw A., 1964, *ARA&A*, **2**, 213
- Boyajian T. S., et al., 2012, *ApJ*, **757**, 112
- Breitschwerdt D., Feige J., Schulreich M. M., Avillez M. A. D., Dettbarn C., Fuchs B., 2016, *Nature*, **532**, 73
- Bressan A., Marigo P., Girardi L., Salasnich B., Dal Cero C., Rubele S., Nanni A., 2012, *MNRAS*, **427**, 127
- Cánovas H., et al., 2019, *A&A*, **626**, A80
- Cardelli J. A., Clayton G. C., Mathis J. S., 1989, *ApJ*, **345**, 245
- Chaikin E., Kaurov A. A., Fields B. D., Correa C. A., 2022, *MNRAS*, **512**, 712
- Chen Y., Girardi L., Bressan A., Marigo P., Barbieri M., Kong X., 2014, *MNRAS*, **444**, 2525
- Cook N. J., Scholz A., Jayawardhana R., 2017, *AJ*, **154**, 256
- Damiani F., Prisinzano L., Pillitteri I., Micela G., Sciortino S., 2019, *A&A*, **623**, A112
- David T. J., Hillenbrand L. A., Gillen E., Cody A. M., Howell S. B., Isaacson H. T., Livingston J. H., 2019, *ApJ*, **872**, 161
- Ekström S., et al., 2012, *A&A*, **537**, A146
- Esplin T. L., Luhman K. L., 2020, *AJ*, **159**, 282
- Feiden G. A., 2016, *A&A*, **593**, A99
- Forbes J. C., Alves J., Lin D. N. C., 2021, *Nature Astronomy*, **5**, 1009
- Fry B. J., Fields B. D., Ellis J. R., 2016, *ApJ*, **827**, 48
- Fuchs B., Breitschwerdt D., de Avillez M. A., Dettbarn C., Flynn C., 2006, *MNRAS*, **373**, 993
- Gaczowski B., et al., 2017a, *A&A*, **608**, A102
- Gaczowski B., et al., 2017b, *A&A*, **608**, A102
- Gaia Collaboration et al., 2016, *A&A*, **595**, A1
- Gaia Collaboration et al., 2018, *A&A*, **616**, A1
- Gaia Collaboration Brown A. G. A., Vallenari A., Prusti T., de Bruijne J. H. J., Babusiaux C., Biermann M., 2020, arXiv e-prints, p. arXiv:2012.01533
- Garrison R. F., 1967, *ApJ*, **147**, 1003
- Gontcharov G. A., 2012, *Astronomy Letters*, **38**, 694
- Gupta A., Chen W.-P., 2022, *AJ*, **163**, 233
- Hiltner W. A., Garrison R. F., Schild R. E., 1969, *ApJ*, **157**, 313
- Hoogerwerf R., de Bruijne J. H. J., de Zeeuw P. T., 2000, *ApJ*, **544**, L133
- Ivezić Ž., Connelly A. J., VanderPlas J. T., Gray A., 2014, *Statistics, Data Mining, and Machine Learning in Astronomy*. Princeton University Press
- Kerr R. M. P., Rizzuto A. C., Kraus A. L., Offner S. S. R., 2021, *ApJ*, **917**, 23
- Kraus A. L., Tucker R. A., Thompson M. I., Craine E. R., Hillenbrand L. A., 2011, *ApJ*, **728**, 48
- Krause M. G. H., et al., 2018, *A&A*, **619**, A120
- Kroupa P., 2001, *MNRAS*, **322**, 231
- Lindgren L., et al., 2018, *A&A*, **616**, A2
- Lindgren L., et al., 2021, *A&A*, **649**, A2
- Lodieu N., Dobbie P. D., Cross N. J. G., Hambly N. C., Read M. A., Blake R. P., Floyd D. J. E., 2013, *MNRAS*, **435**, 2474
- Lodieu N., Smart R. L., Pérez-Garrido A., Silvotti R., 2019, *A&A*, **623**, A35
- Luhman K. L., 2022, *AJ*, **163**, 24
- Luhman K. L., Esplin T. L., 2020, *AJ*, **160**, 44
- Luhman K. L., Herrmann K. A., Mamajek E. E., Esplin T. L., Pecaut M. J., 2018, *AJ*, **156**, 76
- Luri X., et al., 2018, *A&A*, **616**, A9
- Mamajek E. E., 2016, *Proceedings of the International Astronomical Union*, **10**, 21
- Marigo P., et al., 2017, *ApJ*, **835**, 77
- Miller J. A., Fields B. D., 2022, *ApJ*, **934**, 32
- Miller J. A., et al., 2022, arXiv e-prints, p. arXiv:2209.03497
- Miroshnichenko A. S., et al., 2013, *ApJ*, **766**, 119
- Neuhauser R., Giebler F., Hambaryan V. V., 2020, *MNRAS*, **498**, 899
- North J. R., Davis J., Tuthill P. G., Tango W. J., Robertson J. G., 2007, *Monthly Notices of the Royal Astronomical Society*, **380**, 1276–1284
- Ohnaka K., Hofmann K. H., Schertl D., Weigelt G., Baffa C., Chelli A., Petrov R., Robbe-Dubois S., 2013, *A&A*, **555**, A24
- Pecaut M. J., Mamajek E. E., 2013, *ApJS*, **208**, 9
- Pecaut M. J., Mamajek E. E., 2016, *MNRAS*, **461**, 794
- Pecaut M. J., Mamajek E. E., Bubar E. J., 2012, *ApJ*, **746**, 154
- Pedregosa F., et al., 2011, *Journal of Machine Learning Research*, **12**, 2825
- Perryman M. A. C., et al., 1998, *A&A*, **331**, 81
- Pillitteri I., Wolk S. J., Chen H. H., Goodman A., 2016, *A&A*, **592**, A88
- Planck Collaboration et al., 2011, *A&A*, **536**, A24
- Poleski R., 2013, arXiv e-prints, p. arXiv:1306.2945
- Pöppel W. G. L., Bajaja E., Arnal E. M., Morras R., 2010, *A&A*, **512**, A83
- Preibisch T., Mamajek E., 2008, *The Nearest OB Association: Scorpius-Centaurus (Sco OB2)*. The Southern Sky ASP Monograph Publications, p. 235
- Preibisch T., Zinnecker H., 1999, *AJ*, **117**, 2381
- Publication E. S., ed. 1997, *The HIPPARCOS and TYCHO catalogues. Astrometric and photometric star catalogues derived from the ESA HIPPARCOS Space Astrometry Mission* ESA Special Publication Vol. 1200
- Robitaille J. F., Scaife A. M. M., Carretti E., Haverkorn M., Crocker R. M., Kesteven M. J., Poppi S., Staveley-Smith L., 2018, *A&A*, **617**, A101
- Siess L., Dufour E., Forestini M., 2000, *A&A*, **358**, 593
- Skiff B. A., 2009, *VizieR Online Data Catalog*.
- Skrutskie M. F., et al., 2006, *The Astronomical Journal*
- Sørensen M., Svensmark H., Gråe Jørgensen U., 2017, arXiv e-prints, p. arXiv:1708.08248
- Squicciarini V., Gratton R., Bonavita M., Mesa D., 2021, *MNRAS*, **507**, 1381
- Sullivan K., Kraus A., 2021, arXiv e-prints, p. arXiv:2103.09840
- Tetzlaff N., Neuhauser R., Hohle M. M., 2011, *MNRAS*, **410**, 190
- Tokovinin A., 2018, *ApJS*, **235**, 6
- Wallner A., et al., 2016a, *Nature*, **532**, 69

- Wallner A., et al., 2016b, [Nature](#), **532**, 69
- Wilkinson S., Merín B., Riviere-Marichalar P., 2018, [A&A](#), **618**, A12
- Wright N. J., 2020, [New Astron. Rev.](#), **90**, 101549
- Wright N. J., Mamajek E. E., 2018, [MNRAS](#), **476**, 381
- de Geus E. J., 1992, [A&A](#), **262**, 258
- de Zeeuw P. T., Brown A. G. A., de Bruijne J. H. J., Hoogerwerf R., Lub J., Le Poole R. S., Blaauw A., 1997, in Bonnet R. M., et al., eds, ESA Special Publication Vol. 402, Hipparcos - Venice '97. pp 495–500 ([arXiv:astro-ph/9707089](#))
- de Zeeuw P. T., Hoogerwerf R., de Bruijne J. H. J., Brown A. G. A., Blaauw A., 1999, [AJ](#), **117**, 354
- van Leeuwen F., 2007, [A&A](#), **474**, 653

## APPENDIX A: COORDINATE AND SPACE TRANSFORMATIONS

A kinematic group (KG) is defined as a group of stars with a similar space velocity, so we can identify them with over densities in the (U,V,W) velocity space. Moreover, it is useful to define a KG's barycenter<sup>9</sup> such that a barycenter motion (U, V, W)<sub>bar</sub> can be calculated and taken as the true KG's motion. In order to do this, we closely follow the procedure of [Perryman et al. \(1998\)](#) (see its section 5.1 for details). For clarity, an explanation of the differences in our procedure and the main common steps is sketched below.

We take the equatorial coordinates of the north Galactic pole in the ICRS to be

$$\alpha_G = 192^\circ.85948 \quad (\text{A1})$$

$$\delta_G = +27^\circ.12825 \quad (\text{A2})$$

With this convention ([Publication 1997](#)), we are able to obtain the Galactic proper motion ( $\mu_\ell$ ,  $\mu_b$ ) from the equatorial ICRS proper motion Gaia measurements ( $\mu_{\alpha*} = \mu_\alpha \cos \delta$ ,  $\mu_\delta$ ) by directly performing the rotation:

$$\begin{pmatrix} \mu_\ell \\ \mu_b \end{pmatrix} = \frac{1}{\cos b} \begin{pmatrix} a_1 & a_2 \\ -a_2 & a_1 \end{pmatrix} \begin{pmatrix} \mu_{\alpha*} \\ \mu_\delta \end{pmatrix} \quad (\text{A3})$$

With  $a_1$ ,  $a_2$  and  $\cos b$  are given by

$$a_1 = \sin \delta_G \cos \delta - \cos \delta_G \sin \delta \cos(\alpha - \alpha_G) \quad (\text{A4})$$

$$a_2 = \cos \delta_G \sin(\alpha - \alpha_G) \quad (\text{A5})$$

$$\cos b = \sqrt{a_1^2 + a_2^2} \quad (\text{A6})$$

See [Poleski \(2013\)](#) for a detailed derivation. Then, the tangential velocity components can be calculated as:

$$\begin{pmatrix} V_\ell \\ V_b \end{pmatrix} = \frac{Ck}{\pi} \begin{pmatrix} \mu_\ell \\ \mu_b \end{pmatrix} \quad (\text{A7})$$

where  $C=4.74047 \text{ km yr s}^{-1}$  is the conversion constant,  $k$  is the Doppler correction factor, that we take here as 1, and  $\pi$  denotes the parallax measurement, which in our case have formal errors  $< 10\%$ , moreover, this last allows us to obtain an estimate of the distance  $D$  to a star with the approximation  $D \approx 1000/\pi$ , where  $\pi$  is given in mas. Then, the barycentric position for each star and its velocity components in Galactic coordinates can be obtained with:

$$\begin{pmatrix} X \\ Y \\ Z \end{pmatrix} = R \begin{pmatrix} 0 \\ 0 \\ D \end{pmatrix} \quad (\text{A8})$$

$$\begin{pmatrix} U \\ V \\ W \end{pmatrix} = R \begin{pmatrix} V_\ell \\ V_b \\ V_R \end{pmatrix} \quad (\text{A9})$$

where  $R$  is the rotation matrix:

$$R = \begin{pmatrix} -\sin \ell & -\sin b \cos \ell & \cos b \cos \ell \\ \cos \ell & -\sin b \sin \ell & \cos b \sin \ell \\ 0 & \cos b & \sin b \end{pmatrix} \quad (\text{A10})$$

Then, the KG's barycenter and barycenter motion can be via the distribution that models the data. We note here that the main limitation in the (U, V, W) analysis is the incompleteness of  $V_r$  measurements in the Gaia-eDR3 catalog. In fact, in our Main Sample only  $\sim 13\%$  of the stars have  $V_r$  measurements ( $14 \lesssim \text{Gmag} \lesssim 7$ ). Therefore, it is necessary to define a space that gives us information about the true velocity space clustering when no  $V_r$  is available. For this we make use of the observed tangential velocity ( $V_\ell, V_b$ ) and the information obtained from the clustering for stars with  $V_r$  measurements by defining the  $V_{T \text{ exp}}$  space as the expected tangential velocity as a function of sky position given a true barycenter space motion, this is:

$$V_{T \text{ exp}} = \begin{pmatrix} V_\ell \\ V_b \end{pmatrix}_{\text{exp}} = T' \begin{pmatrix} U \\ V \\ W \end{pmatrix}_{\text{bar}} \quad (\text{A11})$$

where  $T'$  is:

$$T' = \begin{pmatrix} -\sin \ell & \cos \ell & 0 \\ -\sin b \cos \ell & -\sin b \sin \ell & \cos b \end{pmatrix} \quad (\text{A12})$$

Finally we choose the transformed space  $V_{T*}$  to perform our clustering analysis. As Upper Scorpius is near, expands a large area in the sky and we aim to distinguish its spatial and velocity substructures, doing our analysis in this space becomes necessary, so that we can minimize projection and perspective effects.

## APPENDIX B: BAYESIAN INFORMATION CRITERIA

We base the selection of the number of components for each GM in the Bayesian Information Criteria (BIC). The BIC yields information about the goodness of fit for a range of number on components. In [Fig.B1](#) we show the BIC for the first 9 components for each GM fit. In the First fit we chose 6 components as it is the global minimum. In the Second fit we chose the first significant local minimum, as larger number of components could yield a lower BIC, but this would compromise us with over fitting the data. In the Third fit the 3 components are chosen because 3 is the global minimum and the most simple case.

<sup>9</sup> Formally, the center of mass instead of the barycenter should be obtained, but the barycenter approximation does no change the results in a significant way ([Perryman et al. 1998](#), [Lodieu et al. 2019](#)).

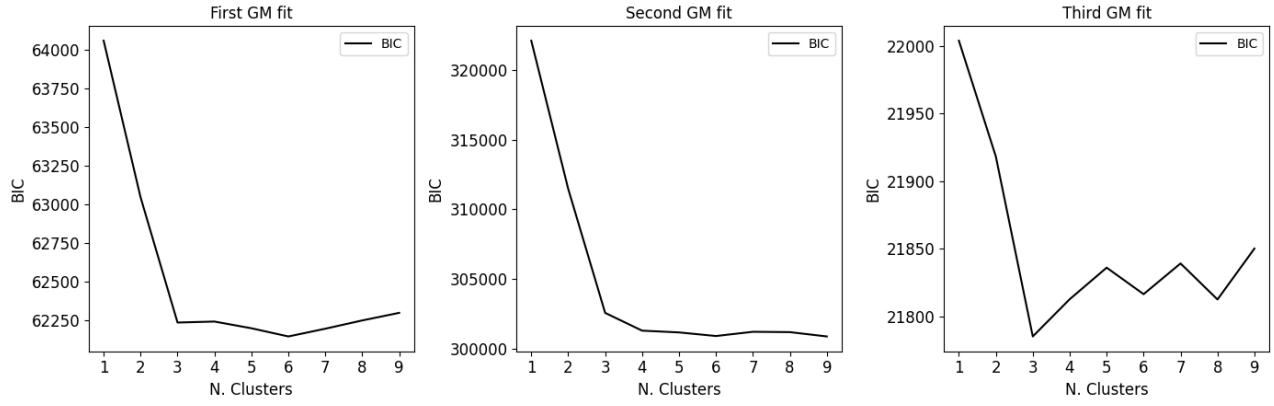


**Figure B1.** BIC for the First, Second and Third GM fits. 3, 4 and 3 components are chosen for these fits based on this plots.